2019

ELECTRO-OPTIC ANTENNA ELEMENTS FOR PASSIVE PHASED ARRAY RADAR

Evan Gawron
Michigan Technological University, ejgawron@mtu.edu

ELECTRO-OPTIC ANTENNA ELEMENTS FOR PASSIVE PHASED ARRAY RADAR

By

Evan John Gawron

A THESIS

Submitted in partial fulfillment of the requirements for the degree of

MASTER OF SCIENCE

In Electrical Engineering

MICHIGAN TECHNOLOGICAL UNIVERSITY

2019

This thesis has been approved in partial fulfillment of the requirements for the Degree of MASTER OF SCIENCE in Electrical Engineering.

Department of Electrical and Computer Engineering

Thesis Advisor:	*Dr. Christopher T. Middlebrook*
Committee Member:	*Dr. Durdu Guney*
Committee Member:	*Dr. Miguel Levy*
Committee Member:	*Dr. Warren Perger*
Department Chair (Interim):	*Dr. Glen Archer*

Dedication

This thesis is dedicated in loving memory of my father, Mark Gawron; also to my Mother, Jody, and my sister, Natalie. None of the work I have done would have been possible without their love and support.

Table of Contents

List of figures

List of tables

Preface

The research presented in this thesis is part of a larger, ongoing research project being performed by members of our research group at Michigan Technological University in collaboration with the Naval Surface Warfare Center (NSWC) Crane. Group members who have been involved in this project include faculty advisor Dr. Christopher Middlebrook and researchers Derek Burrell, Michael Briseno, Dr. Arash Hosseinzadeh, and Michael Maurer.

No section of this thesis is currently published elsewhere. There is intent to publish the waveguide loss and ellipsometry measurements of Chapter 2 in a journal article.

The fabrication recipe used in this work was originally developed by Dr. Arash Hosseinzadeh, with slight modification by Michael Briseno and myself. Poling of EO antenna elements was performed in collaboration with Michael Briseno and Micheal Maurer. Ellipsometry measurements and measurement of poled r_{33} values were performed in collaboration with Michael Maurer. Michael Maurer further assisted with running BeamPROP simulations to verify the single mode condition and negligible electrode loss of fabricated waveguides.

The data collection and analysis for the direction finding proof-of-concept are my own work. The design and simulation of the push-pull EO antenna is original, though Michael Maurer contributed to the optimization of the corresponding finite element simulations.

Acknowledgements

I give my deepest thanks to many people who have helped me to survive and succeed in graduate school.

The staff of the ECE Department at Michigan Technological University has been wonderfully kind and supportive of me throughout the last 2.5 years. Special thanks to Joan Becker, Michele Kamppinen, Mary Ann Wilcox, Lisa Hitch, and Megan Williamson for answering my administrative questions and helping me navigate the logistical side of Michigan Tech. Special thanks also to Mark Sloat and Chuck Sannes for providing me with the tools and practical advice needed to complete my research. I would also like to acknowledge my fellow grad student, Wyatt Adams, for his great insight to the inner workings of COMSOL.

My appreciation also goes to my committee for the time and effort they put into reviewing my thesis: Dr. Durdu Guney, Dr. Miguel Levy, and Dr. Warren Perger.

Much of this thesis is based on devices fabricated in the Microfabrication Facility at Michigan Tech. I am grateful to the facility and especially to Dr. Chito Kendrick for all his support and advice regarding the bizarre things Mike and I wanted to try with the equipment.

A huge thank you to Kevin Kellar and NSWC Crane for conceiving of this project and for the continued financial support of the project.

I have been exceptionally fortunate to work with one of the hardest-working research groups on campus. I could not ask for better co-workers; thank you all! Mike Briseno – for training me in at the very beginning. Dr. Arash Hosseinzadeh, for imparting your deep knowledge and photonics wisdom to the rest of us. Ali Moazzam, for being a great office mate and PCB fabrication expert. And especially Mike Maurer who has been may partner in crime for the last 2 years. He has continually sharpened me into a better researcher and always has an open ear when I need someone to bounce ideas off of.

A deep thank you also goes to Dr. Glen Archer for giving me the initial doorway into Michigan Tech, for keeping me well-employed as a GTA, and for providing excellent mentorship in my journey as a GTA. Passing the information of a prospective grad student along to a few other professors in an email is a very simple thing, but I would not be here without that small action.

Above everyone else at Michigan Tech, I want to thank my advisor, Dr. Christopher Middlebrook for taking me on as a grad student at the beginning, for constantly driving me onward and holding me to the highest standards, and for the trust and confidence that he placed in me.

Lastly, I need to thank my both my immediate and extended families for their continual love and unwavering belief in my abilities throughout this entire grad school journey.

No man is an island. I could not have made it to this point without all of these people.

List of abbreviations

ADC	Analog-to-Digital Converter
AoA	Angle of Arrival
ASK	Amplitude Shift Keying
BPSK	Binary Phase Shift Keying
DF	Direction Finding
E-field	Electric Field
EMW	Electromagnetic Waves
EO	Electro-Optic
EWBE	Electromagnetic Waves, Beam Envelope
FEA	Finite-Element Analysis
IF	Intermodulation Frequency
LNA	Low-Noise Amplifier
LO	Local Oscillator
MZI	Mach-Zehnder Interferometer
QAM	Quadrature Amplitude Modulation
QPSK	Quadrature Phase Shift Keying
RF	Radio Frequency
RIE	Reactive Ion Etch
Rx	Receiver
TE	Transverse Electric
TM	Transverse Magnetic

Abstract

Passive phased antenna arrays are utilized in military and civilian radar systems to determine the received signal origination. Phased array placement for optimal reception is challenging due to the required supporting electronic hardware and the associated coaxial cabling that typically accompanies each antenna channel. Low noise amplifiers and frequency conversion hardware add size and complexity, limiting possible positions for phased array placement. Eliminating required phased array electronic subcomponents without sacrificing function would allow placement onto smaller agile platforms, such as unmanned systems and rapid deployment networks. Electro-optic (EO) antenna elements utilize an optical waveguide embedded between the antenna and ground plane that responds to the electric field received by the resonating antenna. Using EO antenna elements removes associated electronic hardware from antenna sites, thus simplifying advanced phased array technology. EO antenna elements modulate received signals directly into the optical domain where the low loss, electromagnetic immunity, low weight, and small size advantages of optical fiber can be utilized for antenna remoting. The combination of optical signals from EO antenna elements in Mach-Zehnder interferometers reduces the number of overall channels needed for a given radar system. The reduction of channels further serves to decrease the size, weight, cost, computation, and power requirements of the radar system.

This thesis details the design, fabrication, and characterization of EO phased arrays and prototype EO antenna elements, both as individual antenna elements and in a phased array configuration. Waveguide loss, refractive index, and EO coefficient measurements are made for individual EO antenna elements. Radio Frequency (RF) phase modulation emulating a changing angle of arrival is applied by direct injection to a two-element phased array of EO antenna elements. The system's optical output is correlated to the array factor for a two-element phased array showing proof-of-concept that EO antenna elements can be used in direction finding applications. The sensitivity of EO antenna elements is analyzed and a new design for EO antenna elements with improved sensitivity is presented. The electric field distribution of a rectangular patch antenna at resonance was found to be useful for driving a push-pull Mach-Zehnder modulator, doubling the EO antenna element sensitivity.

1 Introduction

Direction finding (DF) is the core function of passive radar systems. Based on the signal received by an antenna or antenna array, radar systems determine the direction from which a radiated electrical signal originated and relay that information to the user. DF techniques are widely used in navigation, military intelligence systems, advanced communication systems, astronomic research, and show promise for autonomous vehicle guidance [1, 2]. Phased array technology is commonly used for DF in radar systems over simpler antennas requiring mechanical rotation due to the improved resolution and lack of mechanical hardware required for rotation [1, 3]. Passive phased arrays of antennas sense phase shifts between spatially displaced antenna elements and correlate them to the direction from which the signal originated.

When designing a passive radar system it is desirable to place phased arrays in a position where they will receive the strongest signal. However, the losses and bandwidth limitations associated with coaxial cabling limit the available locations where it may be practical to place conventional phased arrays within a given application. Coaxial cable is known to have high loss, particularly at carrier frequencies used in radar and communication systems [4, 5]. Furthermore, coaxial cable loss increases with frequency [4, 5]. For example, the low-loss CBL-CU195 cable has specified losses ranging from 65 dB/km (30 MHz) to 981 db/km (5.8 GHz) [6].

Conventional phased array systems compensate for the loss in coaxial cabling by adding low-noise amplifiers (LNA) and frequency conversion hardware to the antenna site as shown in Figure 1.1A. Signals received by phased array antennas can be very weak, requiring LNAs to boost the raw signal amplitude before processing. Frequency converters utilize local oscillators (LO) to down-convert the signal to a lower intermodulation frequency (IF) that can then be transmitted over coaxial cabling with less loss [5]. Along with the receiving antenna, the LNAs and frequency converters make up the front-end hardware of a receiver channel, shown in Figure 1.1. The drawback to all of this hardware is that it adds size, weight, cost, and power consumption to the antenna site and the radar system [7]. Phased arrays can contain many channels, compounding the size, weight, cost, and power required since each channel needs both an LNA and frequency converter. The positioning options available to a phased array within a larger system are thereby constrained by the power routing, size, and weight of the front-end hardware that accompanies conventional phased arrays.

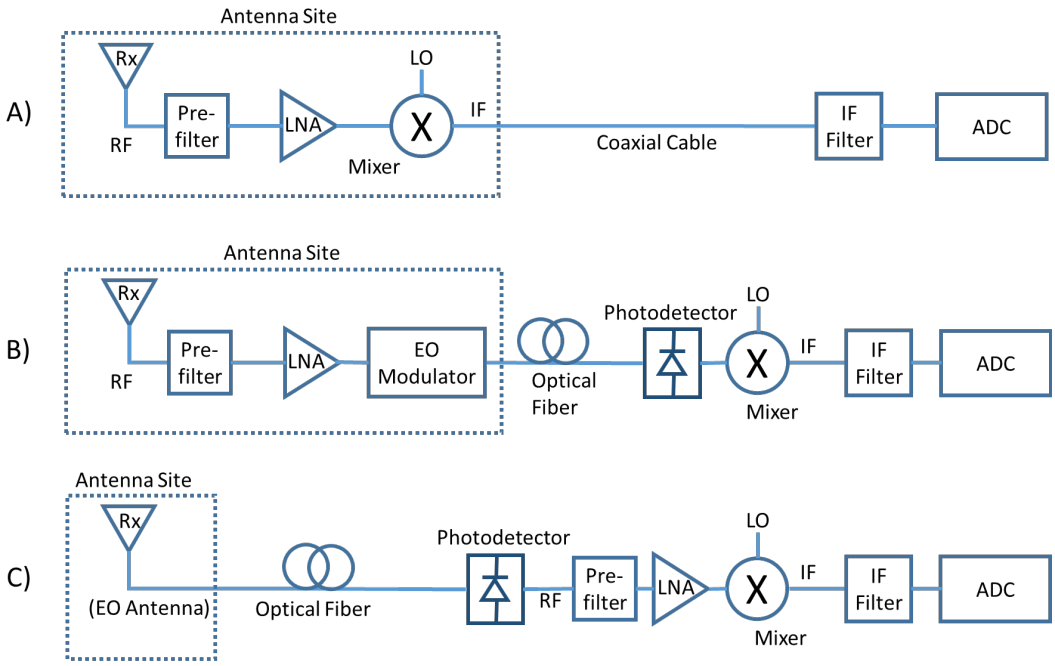

Figure 1.1 Comparison of single channels for carrying RF signals from the antenna site. A) Conventional electrical channel. B) Typical optical antenna remoting with EO modulator. C) Antenna remoting with an EO antenna element.

By using optical fiber and EO modulators, optical antenna remoting is an effective method to carry high-frequency RF signals from an antenna site with little loss. Optical antenna remoting additionally removes frequency conversion hardware from the antenna site as can be seen in Figure 1.1B [7]. Instead of the coaxial copper cabling commonly used in conventional phased array systems, optical antenna remoting employs optical fiber, which has significantly less signal attenuation. Common optical fibers, such as SMF-28, experience less than 0.18 dB/km of loss at 1550 nm [8]. Optical fiber is additionally beneficial in that it is much smaller and lighter than coaxial cable [4]. While optical antenna remoting leads to significant hardware reduction at the antenna site, LNAs typically remain because they are needed to enhance the sensitivity of the receiving antenna [9, 10].

Antenna elements that are integrated with electro-optic (EO) waveguides have the potential to improve and advance radar front ends in several ways, but most notably by removing LNAs from the antenna site. The low loss in optical fiber [4, 5, 8] allows for the transmission of weak signals over fiber so that LNAs may be removed from the antenna site as shown in Figure 1.1C. However, for EO antennas to be practical, they must be sensitive enough that removing the LNA from the antenna site does not appreciably degrade overall receiver sensitivity. The sensitivity of EO antenna elements as it relates to receiver sensitivity has not been evaluated in the existing literature, but it is ultimately tied to the strength of the EO effect inside an EO antenna. The EO effect modulates the refractive index of a material in response to an applied electric field. When the electric field of an antenna drives an EO waveguide, the antenna signal modulates into the phase

of the light passing though the waveguide. Among EO materials, EO polymers show particular promise for application in EO antenna elements; thin films of electro-optic (EO) polymers can exhibit high (>50 pm/V) EO coefficients [11, 12], boosting the minimum signal strength the EO antenna would otherwise be able to detect. Additionally, integrated EO waveguide devices have a low vertical profile (much less than 1 mm) and small footprint, making them ideal to combine with the planar microstrip antennas commonly employed by phased arrays [13-15].

Removing LNA hardware from an antenna site offers several benefits to radar systems. Most apparent is that the weight of LNA hardware may be redistributed to other locations. Such redistribution of weight is of particular interest in aerospace systems where it may be desirable to place phased arrays on the wing-tips of aircraft without adding significant weight in that location. The lighter weight and reduced form factor of EO phased arrays also make them easier to implement in certain military applications including small, unmanned aircraft or rapidly deployed command centers, where size and weight need to be minimal. Furthermore, with the LNA moved, little to no power is needed at the antenna site since no active components remain. The only electricity that may be needed is the small amount of voltage needed to bias the EO antenna element, but due to the capacitive structure of the EO antenna the current draw and power consumption associated with biasing would be minuscule. With careful device design utilizing an asymmetric Mach-Zehnder interferometer geometry [16, 17], even the bias voltage of the EO antenna can be unnecessary and all electrical cabling running to the antenna could be removed. The reduction of power cabling further decreases the footprint and weight of the phased array front end and drastically increases the number of available locations for placing EO phased arrays.

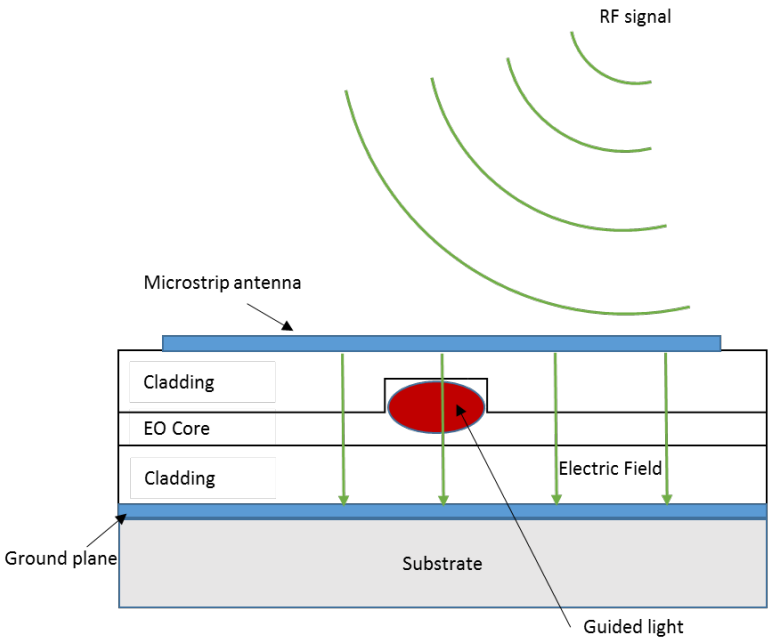

Figure 1.2 Generalized EO antenna element cross-section.

EO antenna elements of various designs have been built and successfully tested, usually for electromagnetic field sensing or communication applications [13, 15, 18-22]. A generalized cross-section showing the structure of an EO antenna element similar to those presented in this thesis is shown in Figure 1.2. Several different microstrip antenna geometries have been utilized in the existing literature on EO antenna elements. EO bowtie antennas [13, 15] and patch antennas [18, 19, 21, 22] seem to be most popular in recent years, though EO tapered dipole antennas have also been constructed [20]. Most of the current designs have antenna electrodes that are in the same plane as the waveguide, rather than the stacked antenna electrode design seen in Figure 1.2. Such planar electrodes require transverse electric (TE) modes inside the EO waveguide to maximize the EO effect. In contrast to this, the EO waveguide elements built for this work were designed to have transverse magnetic (TM) modes that work in conjunction with the stacked electrode design.

Generally, stacked electrode geometry has a more uniform electric field and a greater overlap between the optical mode and applied electric field than the planar electrode geometry [23-25], leading to more efficient EO modulation. Additionally, planar antenna geometries, such as the bowtie design [13, 15], are centered around the EO waveguide with the antenna electrodes extending outward transverse to the waveguide. Since the waveguides are centered with the planar antennas, there is a limit to how closely the waveguides associated with different EO antenna elements can be spaced without the electrodes of the two antenna elements overlapping. If combining multiple EO antenna elements in a single integrated EO phased array, this minimum waveguide spacing requires longer waveguide path lengths to properly reach the planar antennas. The longer waveguide path length will increase optical insertion loss for the waveguides. The stacked electrode design, however, can be paired with rectangular patch antennas to permit closer spacing of EO antenna elements. EO waveguides do not have to be centered with respect to the patch in the stacked electrode geometry and can be shifted around underneath it to minimize the spacing between the waveguides and optimize the electric field strength from the patch antenna. In this way, the stacked electrode geometry can allow greater flexibility in EO phased array design to optimize the optical insertion loss and EO sensitivity.

Arrays of multiple EO antenna elements have also been fabricated and tested on various EO material platforms with electrode geometries requiring both TE and TM waveguide modes [18-21]. A common element of all EO antenna arrays seen in the existing literature is that their EO waveguides have been collinear with several antenna elements such that the phase shifts from all the elements add together [18-21]. Such collinear antenna arrays cannot perform DF as phased arrays since a phase difference between antenna elements is required. Thus, the goal of employing a collinear antenna array along a single waveguide is to extend the interaction length between the optical mode and the received RF signal; thereby maximizing the EO phase shift rather than performing DF measurements. The author is not aware of any prior work developing EO phased arrays for DF applications, making the measurements contained in this thesis the first empirical proof-of-concept that EO antenna elements are capable of finding the AoA for DF measurements.

2 Electro-Optic Antenna Element Design

Numerous factors must to be considered in the design of an EO phased array including antenna design, material characteristics, and optical waveguide design. Chapter 2 addresses these factors in relation to the EO antenna elements that were fabricated and tested for this thesis.

2.1 Rectangular Patch Antenna

Before optical modulation of a signal can occur within an EO antenna element, the antenna must first receive the signal. The antenna's resonant E-field is then used to drive the EO modulation of an optical carrier signal. Rectangular patch antennas are popular for microwave frequencies due to their geometric simplicity and compact, planar form factor [26]. These same characteristics also make them simple to integrate with EO waveguides.

Rectangular patch antenna geometry offers an advantage over other antenna geometries from the existing literature [13, 15, 20] because it has a relatively long active length between the applied electric field and the optical mode in an EO waveguide. Several factors impact the EO modulation efficiency within an EO waveguide, but the most prominent contributing factor that relates to antenna geometry is the active length. Longer active lengths naturally lead to greater EO phase modulation. Builds of EO antenna designs that have been detailed in the existing literature [13, 15, 18-22] include bowtie [13, 15] and tapered dipole [20] geometries which do not modulate the associated EO waveguide along the longest antenna dimension, limiting the active length of the EO waveguide. In contrast to the bowtie and dipole antenna geometries, EO waveguides can run parallel to the longest dimension of a patch antenna, increasing the active length compared to bowtie and tapered dipole antennas operating at similar frequencies. Bowtie [15] and tapered dipole [20] antennas from the existing literature with bandwidths including the X-band have active lengths for a single antenna element of approximately 1.2 mm. For a rectangular patch antenna inside the X-band with a resonant frequency of 10 GHz and dielectric constants ranging from 2.25-28, a range which includes the dielectric constants of common EO materials [27], the active length could range from 2.8-10 mm, several times that of the bowtie or tapered dipole active lengths. The smaller dielectric constants lead to longer active lengths and are typically found with EO polymer materials while EO crystals have much higher dielectric constants [27].

As with all antennas, the rectangular patch resonates with a specific electric field distribution at the resonant frequency. This electric field distribution at resonance is particularly relevant to designing EO antennas to have maximum sensitivity. Placing EO waveguides beneath antenna regions with the strongest electric field makes the most efficient use of the incoming signal power and produces the largest possible EO phase shift for the signal strength received by the patch antenna.

To derive the resonant E-field distribution across a single rectangular patch antenna, the antenna can be modeled as a box-shaped resonant cavity as depicted in Figure 2.1 [28].

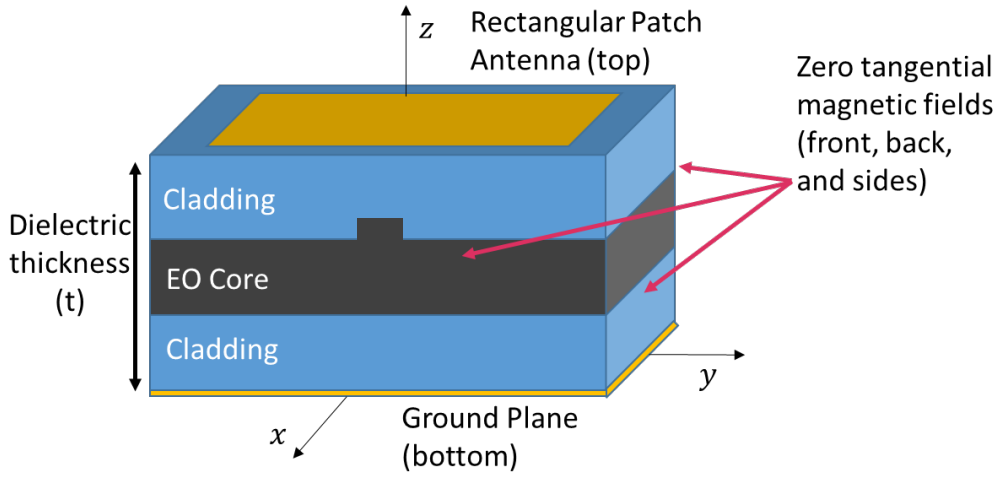

Figure 2.1 Patch antenna geometry with waveguide core and cladding polymer layers.

The cavity is bounded by two conducting surfaces on the top and bottom (the patch and ground plane, respectively). Additionally, the large width-to-thickness ratio of the patch suppresses currents that would generate magnetic fields tangential to the patch edges, establishing zero tangential magnetic field boundary condition fields at the four sides of the patch antenna [28]. With the boundary conditions determined, Equation (2.1), the wave equation, is solved for the vector potential (A_z) eigenmodes of the resonant cavity [28].

$$\nabla^2 A_z + k^2 A_z = 0 \tag{2.1}$$

The dominant mode is associated with the lowest-order frequency and is the only mode considered in this work. For the rectangular patch, this mode is the TM_{100} mode [28]. The only non-zero electric field component for the TM_{100} mode is the z-component, which is given in Equation (2.2) where k_x is the propagation constant of the resonating wave inside the antenna and A_{100} is the vector potential for the TM_{100} mode [28].

$$E_z = -j\frac{k_x^2}{\omega\mu\varepsilon}A_{100}cos(k_x x) \tag{2.2}$$

Therefore, the electric field within a rectangular patch antenna has cosinusoidal variation in the x-direction. In order to meet the resonance condition, the length of the patch in the x-direction needs to be approximately half of the free space wavelength corresponding to the resonant frequency [29]. As shown in the normalized plot of Equation (2.2) in Figure 2.2, the maximum E-field strength for a half-wavelength patch antenna occurs at the edges of the patch. Therefore, EO waveguides should be placed near the edges of the patch antenna in the x-direction to maximize the sensitivity for an EO antenna element.

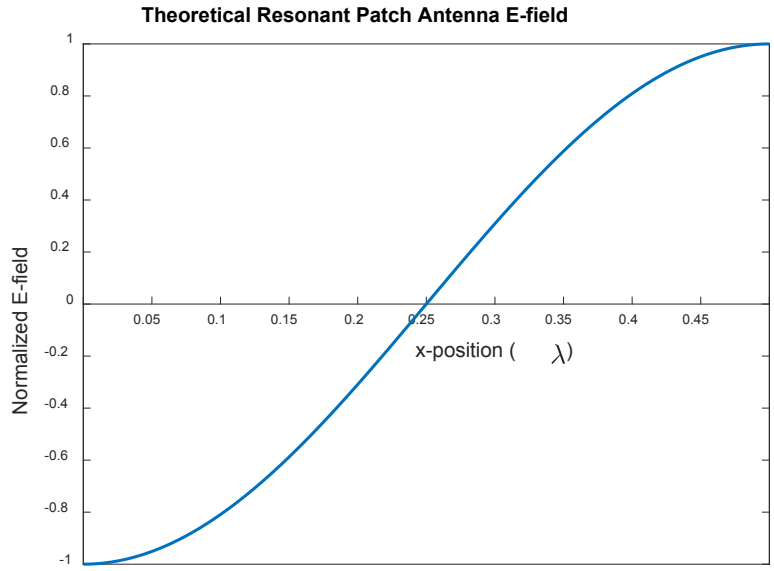

Figure 2.2 Theoretical E-field strength across a rectangular patch antenna at resonance.

The patch antenna used in the design presented herein is a 3 cm square, which places the resonant frequency in the S-band, approximately 3 GHz based on Equation (2.3) where c is the speed of light, L is the patch length, and $\varepsilon_{r\,eff}$ is the effective dielectric constant of the material between the patch and ground plane [26].

$$f_{patch} \cong \frac{c}{2L\sqrt{\varepsilon_{r\,eff}}} \tag{2.3}$$

Since an EO antenna element will require core and cladding layers between the patch and ground plane for waveguides, an effective dielectric constant must be determined to accurately model the multiple dielectric layers. Several methods exist for calculating effective dielectric constants up to 100 GHz by means of weighted averages [30].

Dielectric thickness (t) primarily affects the degree to which fringing fields are present at the radiating edges of the patch antenna. The radiated electric field strength is therefore directly proportional to the dielectric thickness [26]. One of the drawbacks to the rectangular patch antenna is its low radiation efficiency [28]. For EO patch antennas, however, dielectric thickness cannot be changed too freely as a design parameter, since there are numerous designs constraints placed on it related to optical waveguide structure, EO poling efficiency, and waveguide loss. The optical constraints on dielectric thickness are addressed in subsequent sections of this chapter. Based on core and cladding layer thicknesses for optical waveguides, the dielectric thickness for EO antenna element will typically be on the order of tens of micrometers.

2.2 The Electro-Optic Effect

The electro-optic effect provides the link between the resonant E-field received by the patch antenna and the optical output of an EO antenna element; it is the phenomenon by which the refractive index of a material changes with a change in applied electric field. There are two primary electro-optic effects: the Pockels Effect, in which the index of refraction changes linearly with the applied electric field, and the Kerr Effect, in which the index change is proportional to the square of the applied electric field [31]. As is the case for most materials used for EO modulation at low electric field strengths, the EO polymer used in this work has a Kerr coefficient much smaller than the Pockels coefficient, allowing the Kerr effect to be neglected [31]. For an applied electric field along the z-direction (as defined in Figure 2.1) and light polarized parallel to the applied electric field, the change in refractive index is given by Equation (2.4).

$$\Delta n_z = -\frac{{n_z}^3 r_{33} E_z}{2} \tag{2.4}$$

Where n_Z is the refractive index along the z-direction under a zero bias, r_{33} is the EO coefficient in the z-direction and E_Z is the applied electric field strength in the z-direction [32]. Changing the refractive index of the EO-polymer changes the optical path length for light propagating through the material, thereby changing the phase of the light as shown in the exponent of Equation (2.5).

$$E(z,t) = E_0 e^{-\frac{\alpha z}{2}} e^{j(kz[n_z+\Delta n_z]-\omega t)} \tag{2.5}$$

In this manner, a simple waveguide with EO core material sandwiched between two electrodes is a transverse modulator [32] that modulates the phase of the optical signal.

2.3 Electro-Optic Polymer Materials

There are two groups of materials that strongly exhibit the Pockels Effect and are commonly used in integrated EO modulator devices: crystalline and polymer-based EO materials. Most notable among the crystalline material set is Lithium Niobate ($LiNbO_3$), which is widely used in the commercial EO modulators prevalent in fiber-optic communication systems [33]. In recent years, synthetic EO polymers have been developed and experienced significant improvements, leading to a marked increase in achievable EO coefficient.

EO polymers exhibit many advantages over the crystalline EO materials, particularly higher EO coefficients, reduced dispersion between RF and optical frequencies, and simpler integration with semiconductor-based technology [34]. To highlight the merits of the EO polymer used in this body of work, SEO100C, a comparison is made to $LiNbO_3$. The EO coefficient (r_{33}) of $LiNbO_3$ is 30.8 pm/V [32]. Among crystalline EO materials $LiNbO_3$ has the largest r_{33}, but when compared to SEO100C, which has a maximum poled r_{33} of 140 pm/V, it is clear that the polymer has a far more efficient electro-optic response [35]. $LiNbO_3$ has a relatively large dispersion of 3.1 for z-cut crystals, which causes a velocity mismatch between the RF and optical waves, decreasing the EO phase shift as

frequency increases and ultimately limiting the operational bandwidth for $LiNbO_3$ devices to 40 GHz [32-34]. Alternatively, the dispersion between RF and optical frequencies for EO polymers is on the order of 100 times smaller, pushing the maximum bandwidth for polymer-based devices above 100 GHz [27, 36]. For SEO100C specifically, the dispersion between RF and optical frequencies is less than 0.1 [27]. $LiNbO_3$ is difficult to integrate with silicon because it is fragile and its lattice spacing does not match that of silicon [34]. EO polymers such as SEO100C are spin coated into a thin film while in a liquid state and subsequently cured, avoiding the lattice matching and fragility issues seen when adding crystalline EO materials to a silicon substrate.

2.4 Electro-Optic Poling

The EO coefficients of organic EO polymers are based on chromophore molecules with nonlinear optical properties [37]. When an EO polymer is deposited, the chromophores are oriented randomly. Because the Pockels effect depends on materials with a non-centrosymmetric molecular structure, the random orientation of the chromophores results in a negligible EO coefficient [38]. To achieve the maximum possible EO coefficient, a poling process must be performed to align the chromophores. Alignment is achieved by heating the device up to the glass transition temperature of the EO polymer while applying an electric field. As the device nears the glass transition temperature, the molecules become free to rotate. Since the chromophores are polar molecules, they will rotate to align with the electric field as illustrated in Figure 2.3 [38].

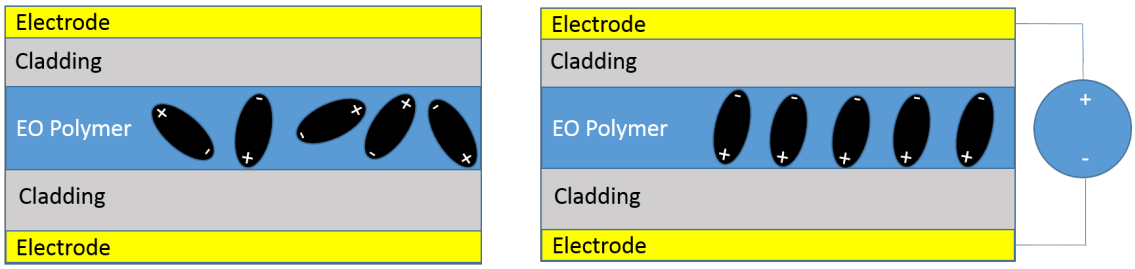

Figure 2.3 Chromophore molecule orientation before poling (left) and during poling process (right).

If the device is cooled back to room temperature with the electric field still applied to the device, the polymer matrix will lock the chromophores into their aligned orientations, giving the EO polymer a non-centrosymmetric structure and an increased EO coefficient [38].

2.5 Rib Waveguide Structure

A waveguiding structure is necessary to control and direct optical signals within an EO antenna element. A rib waveguide structure was used in this study because rib waveguides are relatively simple to fabricate and can be designed to have large single mode

spot sizes, making coupling light into them much easier than equivalent single-mode channel waveguides [39, 40].

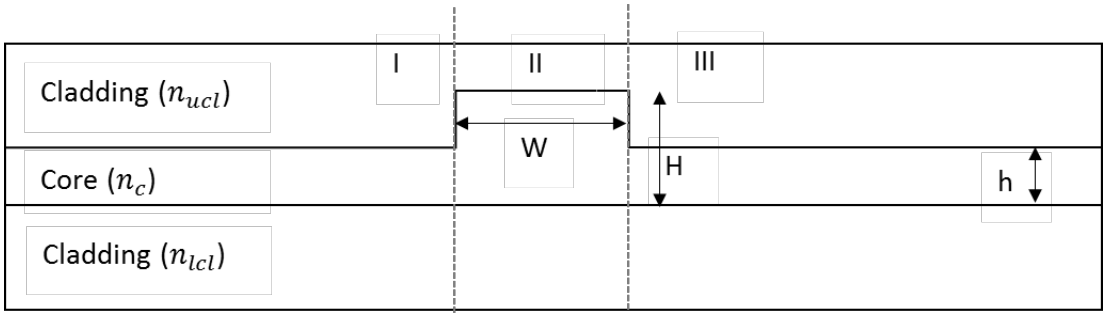

Figure 2.4 Rib waveguide structure.

As with a slab waveguide, the higher refractive index of the core layer confines light in the vertical direction through total internal reflection. The confinement in the horizontal direction can be explained by the effective index method. When the effective index method is applied, the waveguide is divided into three vertical sections (I, II, and III), as shown in Figure 2.4. Each section can be approximated as a slab waveguide. The effective index method accounts for the refractive indices and thicknesses of the three layers. Separate calculations are performed for TE and TM modes. For the stacked electrode geometry of the patch antenna TM modes must be used so the optical E-field aligns with the patch antenna E-field to produce the maximum EO phase shift, as described in Section 2.2. The effective indices of guided modes must be calculated numerically from the TM waveguide equation for dielectric slab waveguides, Equation (2.6), where m = 0, 1, 2,… are the mode numbers, T is the thickness of the core layer, n_{lcl} is the refractive index of the lower cladding, n_{ucl} is the index of the upper cladding, and n_c is the index of the core [25].

$$k_x T = (m+1)\pi - tan^{-1}\left(\left(\frac{n_{lcl}}{n_c}\right)^2\left(\frac{k_x}{\gamma_{lcl}}\right)\right) - tan^{-1}\left(\left(\frac{n_{ucl}}{n_c}\right)^2\left(\frac{k_x}{\gamma_{ucl}}\right)\right) \quad (2.6)$$

The equations for k_x and $\gamma_{lcl,ucl}$ are defined by Equation (2.7). and Equation (2.8) respectively, where n_{eff} is the effective index of the guided mode. In this body of work the top and bottom cladding layers are composed of the same material so $n_{lcl} = n_{ucl}$.

$$k_x = k_0\sqrt{{n_c}^2 - {n_{eff}}^2} \quad (2.7)$$

$$\gamma_{lcl,ucl} = k_0\sqrt{{n_{eff}}^2 - {n_{lcl,ucl}}^2} \quad (2.8)$$

Due to symmetry, the effective indices of region I and region III are identical. In region II, the greater proportion of high-index material raises its effective index. The higher effective index of the guided modes in region II relative to regions I and III creates

a waveguiding effect in the horizontal direction, thereby confining the light to one-dimensional propagation.

2.6 Cladding, Electrode, and Substrate Selection

While the EO polymer used as the core material has already been discussed in Section 2.3, consideration must also be given to the polymer cladding material in the waveguide design. The refractive index of the cladding layer is of primary importance since it must be less than the refractive index of the core layer for total internal reflection to occur inside the waveguide. Furthermore, the refractive index difference between the core and cladding layers determines how confined the optical mode is within a waveguide, impacting waveguide characteristics such as bending loss [25, 41]. For the EO antenna elements studied in this work, the EO polymer SEO100C was used as the waveguide core material and the UV-curable adhesive NOA73 was chosen for the cladding layers. SEO100C and NOA73 have respective refractive indices of 1.65 (1543 nm) [11] and 1.5543 (1550 nm) [42].

Chemical compatibility between the EO polymer and the cladding material is equally critical to the waveguide design. In fabrication, the polymer layers are sequentially spin-coated while in a liquid state and then cured. Therefore, the lower (cured) polymer must not be susceptible to the solvent of the next polymer that is applied. The bottom cladding material cannot be susceptible to the solvent of the EO polymer. Additionally, the solvent of the top cladding material must not attack the cured EO core layer beneath it.

Cladding materials should ideally have relatively low resistivities compared to the resistivity of the EO polymer used for the core layer. The resistances of three polymer layers act as a resistor divider to any voltage applied across them [11]. Keeping the cladding resistivity low maximizes the E-field applied to the EO core material, which is particularly important for poling the EO polymer. If higher-resistivity cladding materials are used instead, the poling voltage must increase in order to maintain the optimal E-field across the core layer. Using poling voltages above 600 V may place devices at an increased risk of dielectric breakdown.

The thickness of the cladding layer is another important design parameter. The metal electrodes of the patch antenna and ground plane will absorb power from the optical mode if the waveguide is not sufficiently isolated by the cladding layers. For this design, cladding layer thicknesses of 4.3 μm were used and found to be sufficiently thick enough to minimize optical absorption loss by the electrodes [24].

The primary concerns surrounding the electrode metal used in an EO antenna element design are that the metal has a high conductivity and that it is practical to deposit with typical microfabrication processes. Gold was used as the material for the top and bottom electrodes of the fabricated design based on its excellent conductivity and standard use in MEMS-scale devices. Gold can be deposited both through sputtering and electron-beam (E-beam) deposition. While both methods are effective, E-beam deposition is done

at a lower temperature and is therefore preferable over sputtering when depositing metal on polymer layers. If a device is heated too much during the electrode deposition process, the polymer layers can become deformed or damaged. Because sputtering directs plasma at the device and the electron beam used to evaporate the metal in an E-beam deposition is far from the device being coated, there is a greater risk of heating the polymer layers associated with sputtering than with E-beam deposition. Additionally, the 3 cm patch antennas from this work have a relatively large electrode areas, making them more sensitive to any deformations that might occur from sputtering than other devices, such as simple MZI modulators with long thin electrodes that are only meant to cover the immediate vicinity of a waveguide (~50 μm width). If sputtering must be used in fabrication, care should be taken to either tightly control any heat transfer from the process or select waveguide materials that are able to withstand the heat.

In addition to the polymer and electrode materials, the substrate material also deserves consideration. Since the waveguides are entirely polymer-based and the substrate merely serves as a platform for the EO antenna element, there is significant flexibility when choosing a substrate material. This opens up the possibility of eliminating the substrate altogether and building EO antenna elements directly on a smooth surface of the system in which they would be used, similar to a conformal coating.

When choosing a substrate on which to fabricate an EO antenna element, roughness and cleanliness are of critical importance. A rough surface may disrupt the waveguides so that little to no light is transmitted and a dirty surface will introduce foreign materials that may disrupt waveguide paths, as well as pose adhesion issues to the lower polymer layer. Fabricating the initial prototype devices on a silicon wafer was a natural choice. Polished silicon wafers are clean, have extremely low average roughness (typically less than 1 nm), and are a standard substrate for MEMS-scale devices.

2.7 Ellipsometric Characterization of SEO100C

Empirical characterization of optical materials is helpful to understanding the behavior of fabricated devices and informative when designing photonic devices. Even though a manufacturer may specify an index of refraction for an optical material, it is important to empirically measure the refractive index to account for any differences in material preparation. Furthermore, the manufacturer of SEO100C only cites a poled refractive index. EO polymers are known to experience a slight change in index through the poling process [11], therefore a measurement of the unpoled refractive index provides more complete knowledge of the material used. Having an accurate measurement of the refractive index for a material also allows for more accurate modeling and design of future waveguide structures.

The refractive index of SEO100C was measured using transmission and reflection ellipsometry performed with a J.A. Woolam VASE Ellipsometer. A sample of unpoled SEO100C was prepared by spin-coating a 2.7 μm film of SEO100C onto an ITO glass slide and curing it in a vacuum oven. For ellipsometry to be effective, the thickness of the film

needed to be on the same order as the desired wavelength [43]. The wavelengths at which the ellipsometry was performed are all within an order of the film thickness under test. The transparent substrate allowed for transmission studies to be conducted in addition to reflection ellipsometry. To improve the accuracy of the reflection ellipsometry results, an area of the back side of the substrate was roughened to eliminate the back reflections from the rear glass/air interface. The samples were measured with an optical profilometer to determine the film thickness and several sets of transmission and reflection ellipsometric data were collected. Knowing the sample thickness, the optical properties were determined by fitting the ellipsometric data.

A bare ITO glass slide was measured to accurately model the substrate on which the SEO100C sample was prepared. Using the base model of the ITO slide, a model was created for the SEO100C sample. The fitting process was performed in the NIR range and SEO100C's refractive index was fit from 1100 nm to 1700 nm, a range that includes the telecommunications wavelengths of 1310 nm and 1550 nm. Datasets from different locations on the sample were simultaneously fit. A Sellmeier equation was used to describe the dispersion curve and fit while matching the thickness of the modeled layer to the measured value. Using the manufacturer's reported refractive index of 1.7 for poled SEO100C, an initial curve was chosen and then incrementally changed to minimize the error between the model and the collected data. The Sellmeier equation is shown in Equation (2.9), with the coefficients listed in Table 2.1. For the listed coefficients the wavelength is given in microns. This fitting process found a refractive index value of 1.655 at 1550 nm, with a mean squared error for the fit that was below 10. The measured dispersion curve of SEO100C is shown in Figure 2.5.

$$n(\lambda) = \sqrt{1 + \frac{B_1\lambda^2}{\lambda^2 - C_1} + \frac{B_2\lambda^2}{\lambda^2 - C_2} + \frac{B_3\lambda^2}{\lambda^2 - C_3}} \tag{2.9}$$

Table 2.1 Sellmeier coefficients for SEO100C

Coefficient	B_1	B_2	B_3	C_1	C_2	C_3
Value	1.3291	0.8924	0.0275	0.3511 μm^2	-13.961 μm^2	1.0832 μm^2

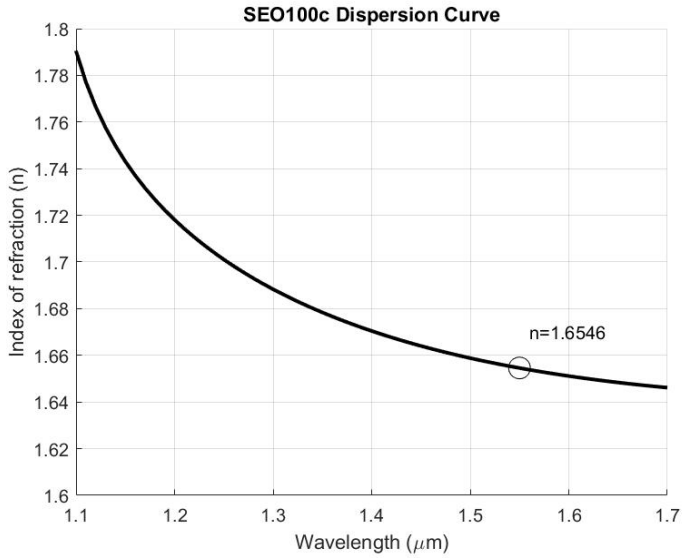

Figure 2.5 Dispersion curve for SEO100C as measured by ellipsometry. The refractive index at 1550 nm is highlighted with a value of 1.655.

The manufacturer specifies two refractive indices at 1550 nm for poled SEO100C films. The unpoled refractive index measurement of 1.655 is 0.045 below the manufacturer's value of 1.7 (TM), but very close to the 1.65 (TE) value [35]. Previous prism coupler measurements taken at 1543 nm determined unpoled refractive indices between 1.64-1.65 for TM light and 1.66 for TE light [11]. The agreement between the ellipsometry and prism coupler results stresses the importance of characterizing the materials used in fabricated devices, and shows the consistency of the mixing process used during fabrication. Furthermore, most device designs will have waveguide sections that are never poled since only the areas of EO polymer between electrodes are poled. Therefore, the unpoled refractive index is needed to accurately model the wave propagation in the unpoled waveguide sections of a given device. Examination into the extinction coefficient revealed it was orders of magnitude below the accuracy of the ellipsometer and was not reported from the collected data.

2.8 Single Mode Condition for Rib Waveguides

Single mode waveguides are preferable in EO antenna elements over multimode waveguides. Multimode waveguides are undesirable to use in EO antenna elements for several reasons. Losses are higher in multimode waveguides than in single mode waveguides. Multimode waveguides also experience dispersion and interference between modes; both effects introduce optical noise to the otherwise stable fundamental waveguide mode. Single mode waveguides are further necessary for the Mach-Zehnder modulators associated with EO antenna elements. Mach-Zehnder modulation is discussed in greater detail in Section 3.1, but it is briefly addressed here as a motivating reason for using single mode waveguides in EO antenna elements.

Mach-Zehnder modulators are designed such that when two coherent phase-shifted signals are combined the resulting interference modulates the output intensity of the light. In the case where a π phase difference is present between the Mach-Zehnder legs, destructive interference occurs and the optical power radiates away from the waveguide into the surrounding material because the antisymmetric mode that would result is not supported by the single mode waveguide at the modulator output [25, 44]. However, if the output waveguide is multimode rather than single mode, it may be large enough to support an interference pattern inside the waveguide. In this case, a π phase difference between the legs will no longer fully extinguish the optical mode. Furthermore, if the legs of the Mach-Zehnder consist of multimode waveguides, dispersion dictates that each mode experiences a slightly different refractive index and acquires a different phase as it propagates, making the intensity modulation resulting from the interference of multimode waveguides less predictable. For these reasons, the dimensions of waveguides fabricated in this study were designed to be single mode.

For a rib waveguide structure, higher-order modes in the rib region can couple into the slab of core material and dissipate perpendicular to the waveguide if the effective index of the fundamental slab mode is higher than the effective index of the higher-order rib waveguide modes [39]. This marks the distinct advantage that rib waveguides can support larger single mode sizes than channel waveguides. The rib waveguide dimensions are noted in Figure 2.4. The waveguide width (W) and the ratio of the slab height (h) to the total core layer thickness (H) of the EO core layer fully define the waveguide dimensions and determine the number of modes present in a rib waveguide for given core and cladding materials. The material set used to fabricate the devices for this thesis was identical to that for the EO waveguide devices in [24] and the calculations performed therein determined the waveguide dimensions at which the fundamental slab mode index equals the first order rib mode index for a TM waveguide. Figure 2.6 shows this border line between single and multimode rib waveguides for waveguides of various slab height ratios (h/H) and rib widths.

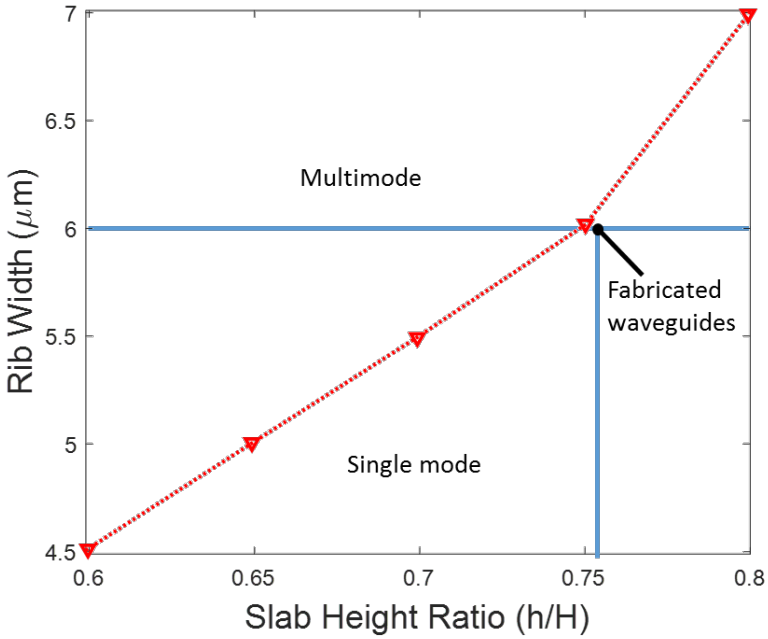

Figure 2.6 Parameter space for single and multimode TM waveguides, as it relates to slab height ratio and rib width [24]. The fabricated rib waveguide dimensions are indicated by the intersection of the blue lines.

A rib width of 6 µm was selected so that the waveguide mode would have a similar size to 6 µm optical fiber that could be used for coupling. A target rib height of approximately 650 nm was also selected to produce single mode waveguides for this rib width. As Chapter 4 will note, the average rib height was measured during fabrication to be 667 nm, prior to applying the top cladding layer. The waveguide width and the total film thickness of the fabricated waveguide are 6 µm and 2.7 µm, respectively [35]. From the etch depth and the total film thickness, the slab height ratio can be determined; for the fabricated waveguides this ratio was 0.753. As noted in Figure 2.6, a slab height ratio of 0.753 at a waveguide width of 6 µm will produce a single mode waveguide. However, these dimensions place the waveguide very near to the threshold of multimode behavior. Therefore, a simulation with RSoft BeamPROP 8.1 software was used to further verify the single mode operation of the fabricated waveguides. The simulation calculated only one propagating TM mode, which is shown in Figure 2.7 alongside the actual mode shape of the waveguide.

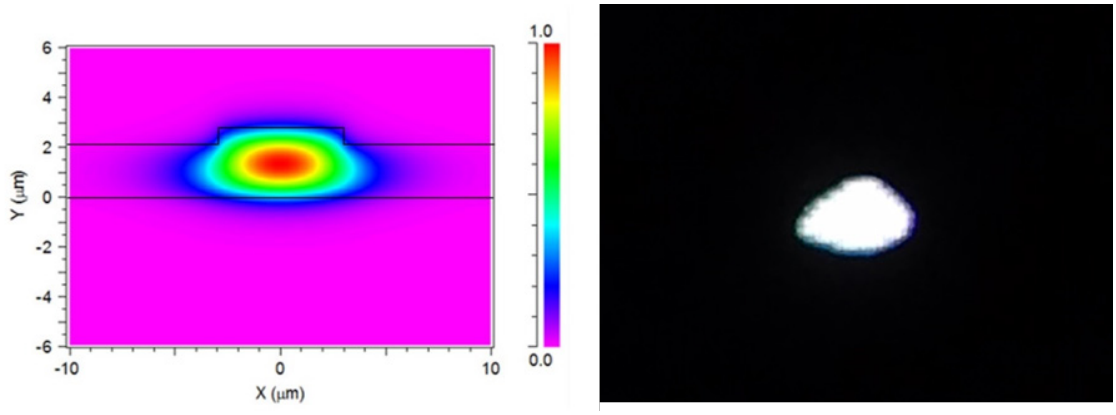

Figure 2.7 Single TM mode simulated in RSoft's BeamPROP software (L) for the fabricated waveguide dimensions and the actual waveguide mode photographed with an IR camera (R).

To obtain the measurement of the mode shape seen in Figure 2.7, laser light at 1545 nm was coupled into a straight waveguide. An objective lens positioned at the waveguide output collimated the light before it was imaged with an IR camera. The resulting image was stable and consisted of only one bright spot that is comparable to the simulated mode.

2.9 Optical Loss Characterization

As with any optical waveguide device, it is desirable to minimize the optical insertion loss of EO antenna elements. Having a large optical insertion loss decreases the signal to noise ratio at the photodetector and impairs the overall sensitivity of the receiver channel. For phased array applications high insertion loss can be especially problematic for detecting weak radiated signals from targets that may be far away. It is therefore of interest to characterize the optical losses of the rib waveguides made from the SEO100C EO polymer in order to evaluate its suitability for use in EO antenna phased array applications. Prior to this study, the overall optical loss of SEO100C within a rib waveguide structure was unknown. To characterize the optical losses, a sample of straight waveguides from the fabricated wafer was analyzed using the cutback method to measure the optical losses native to the fabricated single mode rib waveguide structure.

2.9.1 Components of Optical Waveguide Loss

The insertion loss of an optical waveguide device can be broken into loss contributions stemming from the material properties and the rib waveguide structure. The total insertion loss is described by Equation (2.10).

$$InsertionLoss_{dB} = ScatteringLoss_{dB} + AbsorptionLoss_{dB} + RoughnessLoss_{dB} + CouplingLoss_{dB} + ElectrodeLoss_{dB} \quad (2.10)$$

The first two terms in Equation (2.10) are intrinsic to the waveguiding material. While the roughness loss term in Equation (2.10) is not intrinsic to the material, it is still intrinsic to the waveguide and is due to the sidewall roughness of the core/cladding material interface. Each of the first three terms in Equation (2.10) are dependent on waveguide length [45, 46]. These first three terms comprise the characteristic loss of the waveguide as noted in Equation (2.11).

$$WaveguideLoss_{dB} = ScatteringLoss_{dB} + AbsorptionLoss_{dB} + RoughnessLoss_{dB} \tag{2.11}$$

The last two sources of loss in Equation (2.10) are not characteristic of the waveguide. Coupling loss is the combined loss from the mode mismatch between the optical fibers and the waveguide, reflections at material interfaces, and end face roughness of the waveguides. Electrode loss refers to the optical power loss due to absorption by the metal electrodes. It is determined by the proximity of an electrode to the optical mode and the length over which the electrode is in the vicinity of the waveguide [47]. Electrode loss should not be confused with RF power losses in the transmission line structures sometimes used as travelling wave electrodes for EO modulators.

2.9.2 Ensuring Zero Electrode Loss

Electrode loss must be considered along the entire waveguide length if the ground plane covers the entire wafer area. If the cladding layers are sufficiently thick enough to isolate the optical waveguide mode from the metal electrodes, however, electrode loss can be eliminated. Electrode loss was simulated using BeamPROP 8.1 for waveguides of the same dimensions as the fabricated waveguides, with top and bottom cladding layers of varying thicknesses. The simulation results can be seen in Figure 2.8. At the cladding thickness fabricated, the electrodes contribute 0.018 dB/cm to the overall insertion loss, which is less than 1% of the measured length dependent losses reported in the next section. Therefore, the assumption that absorptive electrode loss is negligible is justified.

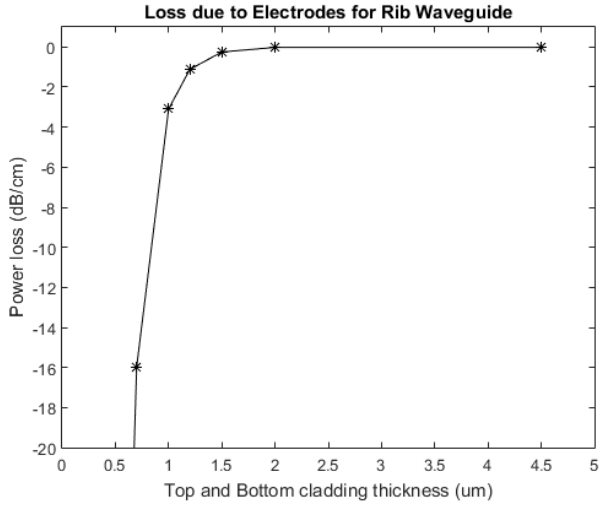

Figure 2.8 Simulated electrode loss for various cladding thicknesses.

2.9.3 Cutback Method Results

Coupling and waveguide losses can be experimentally determined by the cutback method [17]. It is important to be able to distinguish the waveguide loss from the coupling loss, as coupling efficiency can vary depending on the waveguide end face quality and the coupling method used. Unlike waveguide loss, coupling loss is independent of waveguide length and corresponds to the static loss in cutback method data.

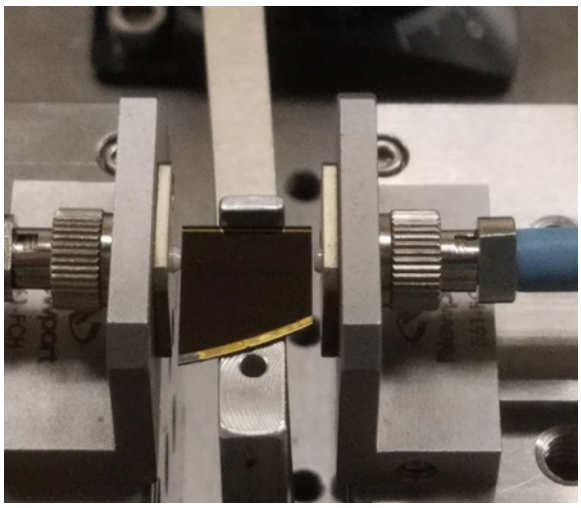

Figure 2.9 Experimental coupling setup. Input fiber is on the right, output fiber is on the left. Fibers were mounted on 3-axis micrometer stages.

To measure insertion loss in the cutback method study, single mode 6 μm fibers were used to couple 1550 nm light into and out of the waveguides (Figure 2.9). The 6 μm fiber mode better matched the 6 μm waveguide mode than modes from the 9 μm fibers more commonly used at 1550 nm. By matching the fiber and waveguide modes more closely, lower coupling loss can be achieved.

The sample used had eight parallel straight rib waveguides fabricated according to the procedure described in the Chapter 4. The waveguide length was measured with calipers, the power from the input fiber was measured, each of the eight waveguides were coupled through, and power from the output fiber was measured. From the input and output fiber power measurements, the insertion loss was determined for each of the eight waveguides. The waveguides were cut back from the output end with a dicing saw so that the input end faces remained unchanged and the output end faces were of consistent quality across all waveguide lengths. After the sample was diced, the measurement process was repeated based on the new length. A linear regression of the insertion loss was performed to characterize the length-dependent losses and coupling losses. Figure 2.10 shows the collected data points with the linear regression. The y-intercept is the average coupling loss due to both the input and output fibers. The total coupling loss was found to be 7.2 ± 0.2 dB. The length-dependent losses were found to be 4.2 ± 0.2 dB/cm. Because electrode

loss is negligible, the length-dependent losses represent the characteristic waveguide loss as defined in Equation (2.11).

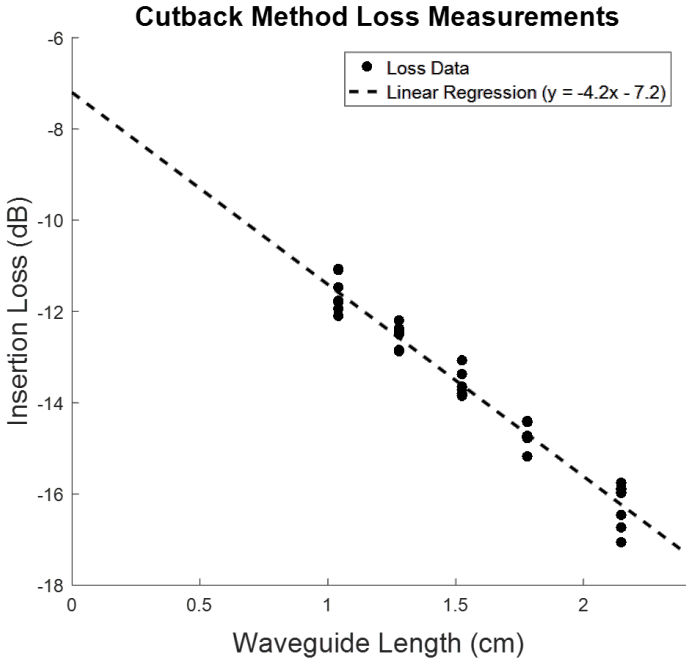

Figure 2.10 Experimental results from the cutback method. Insertion loss of eight waveguides were measured at each waveguide length. Measurements were made at 1550 nm.

Complete knowledge of SEO100C waveguide loss is useful in the design of integrated EO antenna elements and other photonic devices using the SEO100C/NOA73 material set. This becomes particularly relevant when a design balance must be implemented between waveguide and bending losses, such as the S-bends in a Mach-Zehnder modulator or the ring of a ring resonator. Additionally, the loss data gathered here is useful when designing a device's size relative to its insertion loss.

3 Electro-Optic Phased Array Design

Chapter 3 addresses the relevant design considerations for EO phased arrays. Phase-modulated optical signals need to be combined interferometrically to produce an amplitude modulated signal. For integrated waveguide devices, a Mach-Zehnder interferometer is used to perform the conversion to amplitude modulation. Additionally, the spacing between EO antenna elements in a phased array will determine the sensitivity of an array to a change in AoA and its effectiveness at DF. A two-element array design is the most fundamental phased array and is described herein.

3.1 Mach-Zehnder Interferometer

In the context of an EO antenna element, an integrated interferometer of single mode waveguides is necessary to convert the optical phase shift caused by the EO effect into an intensity modulated signal that can then be detected by a photodetector. The most common interferometric structure used to build integrated modulators is the Mach-Zehnder interferometer (MZI). Within the MZI, input light is split in two separate legs. Half of the light travels down the reference leg while half the light travels down the measurement leg. If the phase in the measurement leg changes with respect to the reference leg phase, the two waves will combine constructively or destructively at the output of the interferometer, thereby modulating the intensity of the light. Constructive interference results in maximum transmission from the MZI output. When waves from the MZI legs interfere destructively, they attempt to create an antisymmetric mode, which is not supported by the single mode waveguides of the interferometer. In this case, light radiates out of the waveguide into the cladding and the output power is extinguished [25, 44]. The instantaneous optical amplitude output (transmission, T) from a MZI exhibits a squared-cosinusoidal dependence on the phase difference (ϕ) between the two legs as noted in Equation (3.1) [31].

$$T(\phi) = cos^2\left(\frac{\phi}{2}\right) \tag{3.1}$$

For EO modulation, it is desirable to have a linear relationship such that the output intensity scales with the signal strength of the modulating voltage. In an integrated MZI, this is best achieved by maintaining a steady phase difference of $\pi/2$ between the two legs so that a time-dependent modulation signal can alter the phase along the most linear region of Equation (3.1). In practice, phase biasing is commonly achieved by applying a DC voltage to one leg of the EO MZI. However, phase biasing could also be accomplished by designing asymmetric path lengths between the MZI legs such that the physical path length difference leads to a $\pi/2$ phase difference [16, 17]. Phase biasing by this second method would make it unnecessary to run electrical wiring to an EO antenna element, allowing the device to truly be passive in the sense that it requires zero electrical power from the radar system.

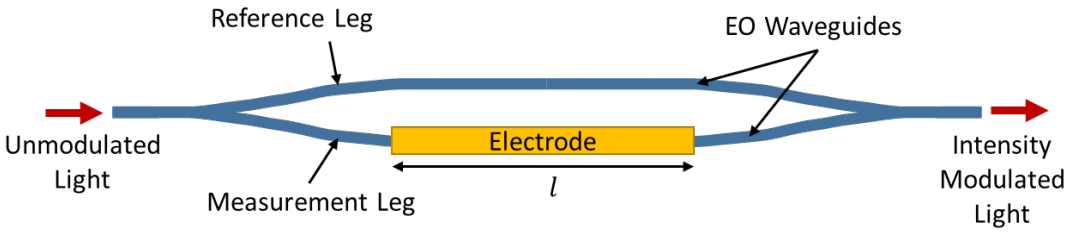

Figure 3.1 Diagram for an integrated Mach-Zehnder interferometer composed of EO waveguides.

The MZI configuration can be built out of optical waveguides with a geometry similar to that shown in Figure 3.1. If these waveguides are made with an electro-optic core material and an electric field is applied to the measurement leg, the measurement leg will acquire a phase shift relative to the reference leg. In this way, the output voltage from a patch antenna can be used to modulate an optical signal.

The half-wave voltage (V_π) of an EO modulator is a metric of modulation efficiency. It is defined as the input voltage required to produce an EO phase shift of π radians. The half-wave voltage is equivalently defined as the voltage required to switch between the maximum and minimum transmitted optical powers as shown in Figure 3.2.

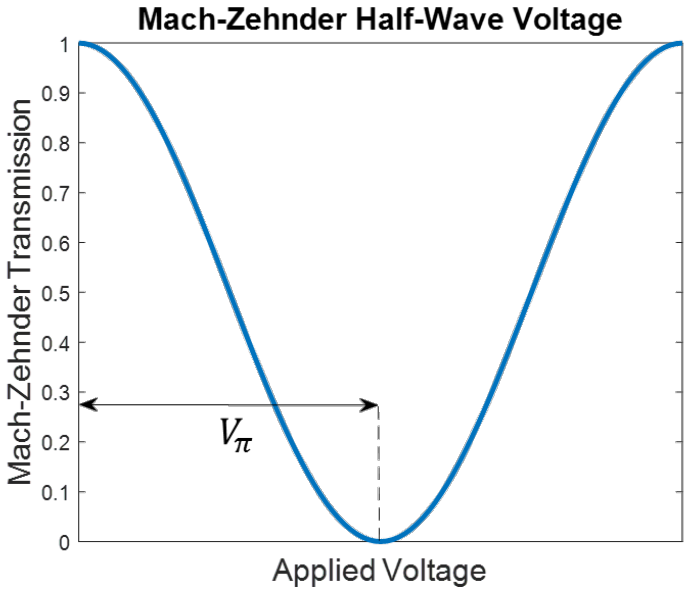

Figure 3.2 Half-wave voltage for a Mach-Zehnder Interferometer.

$$V_\pi = \frac{\lambda t}{{n_e}^3 r_{33} \Gamma_{TM} l} \tag{3.2}$$

The half-wave voltage for a MZI is mathematically defined in Equation (3.2) where λ is the free-space wavelength, n_e is the extraordinary refractive index of the EO material (in this case the refractive index in the z-direction), r_{33} is the EO coefficient, Γ_{TM} is the

overlap integral between the modulating E-field and the portion of the TM optical mode inside the EO polymer, t is the electrode separation distance denoted in Figure 2.1, and l is the length over which the electric field is applied in Figure 3.1.

3.2 Two-Element Phased Array

To demonstrate initial proof-of-concept for utilizing EO antenna elements in passive phased array applications, two EO antenna elements were designed, fabricated, and tested. The phase difference between antenna elements can be used for DF of a RF signal [28]. The relation between the total electric field received by the array and the phase difference between the elements is most simply defined by the antenna array factor. For a two-element array the array factor (AF) is defined by Equation (3.3)

$$AF = cos\left(\frac{1}{2}[k_{RF}\, dcos(\theta) + \beta]\right) \tag{3.3}$$

Where k_{RF} refers to the propagation constant of the incoming RF signal, d is the spacing between the antenna elements, θ is the AoA, and β is a constant phase difference between the two antenna elements [28]. The array factor describes the radiation pattern for the array configuration. Assuming all antennas in the array have the same radiation pattern, the overall radiation pattern of the antenna array can be determined by multiplying the array factor by the radiation pattern of the individual antenna element [28]. The $k_{RF}\, d\, cos(\theta)$ factor in Equation (3.3) refers to the phase difference between the two incoming rays from the RF signal source as shown in Figure 3.3, while β refers to any constant phase difference between the two antennas of the array [28]. Both of these factors are divided by two in Equation (3.3) because half of the phase shift is attributed to the field output from each antenna in the two-element array.

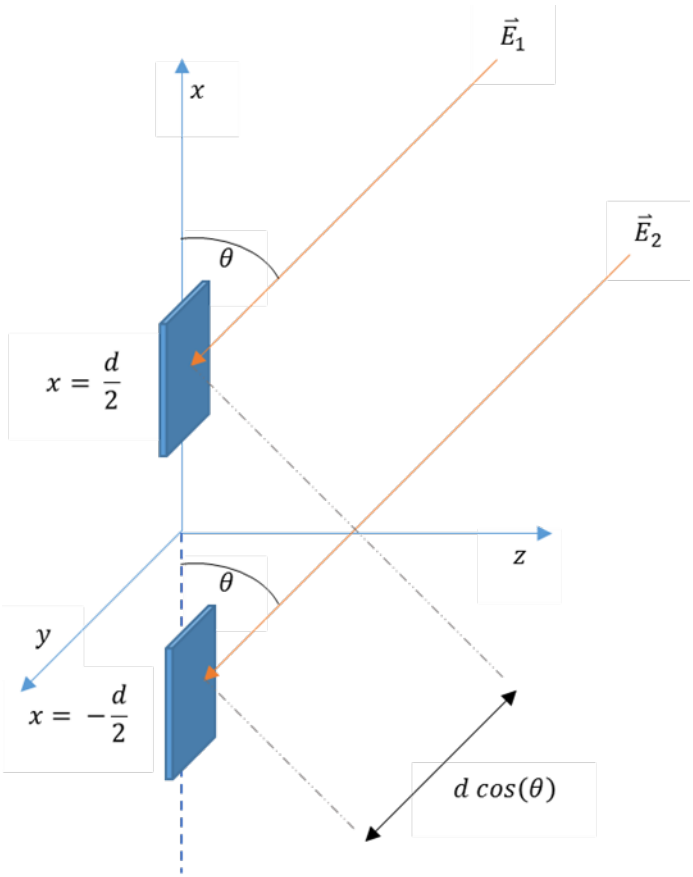

Figure 3.3 Phased array consisting of two patch antennas.

In Figure 3.3, both fields received by the antennas are paraxial and share the same AoA. This is not strictly true, but is a good approximation when the RF source is in the far field as is the case for most phased array applications [28]. Using Equation (3.3), changes in the total signal amplitude received by both antennas can be correlated to the angle of arrival (θ). The constant phase difference between the antennas (β) does not contain information related to the position of the incoming signal; if there are no additional phase shifts between the antenna elements it can be neglected.

The antenna spacing is a critical parameter in the design of a passive phased array for DF applications. Increasing the antenna spacing improves phased array sensitivity to AoA [48]. However, once the spacing passes one half-wavelength the interference between the antennas will create multiple lobes in the array radiation pattern. These lobes create multiple possible AoA for the same phased array output. To avoid such ambiguity, phased array antenna spacing should be kept smaller than one half wavelength of the incoming signal for DF applications [1, 48].

3.3 Integrated EO Phased Array System

EO antenna elements arranged in a simple two-element phased array with EO waveguides configured in a MZI beneath the phased array antenna elements can show proof-of-concept that EO phased arrays can be used in DF applications. Each leg of the interferometer is driven by a different antenna element and the MZI detects the relative phase shift between signals received by the two antennas. When the optical signals from each leg interfere with one another, intensity modulation will result such that the modulation envelope is related to the phase shift between the legs of the MZI. The intensity modulated light can then be detected by a photodetector, which will convert the optical signal into an electrical current. Electrical filters and amplifiers may be used to condition the signal further before it is digitized and the DF computations are performed.

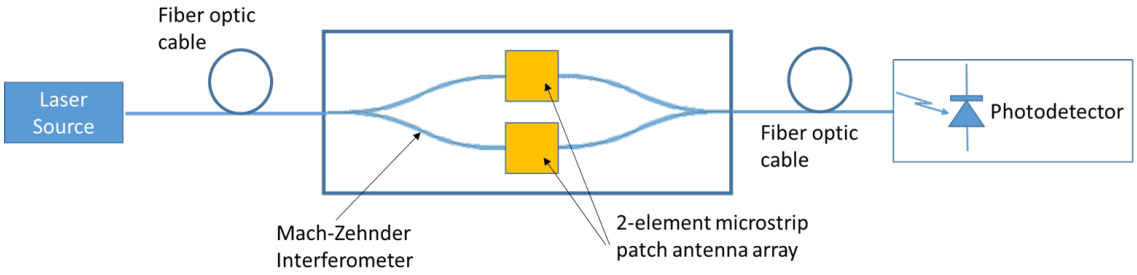

Figure 3.4 Simple two-element phased array with underlying Mach-Zehnder interferometer.

A notable advantage of EO antennas over conventional electrical antennas in the context of phased arrays is the necessary combination of multiple signals in the MZI. In conventional passive phased array DF systems, each antenna requires its own channel and therefore its own LNA, frequency converter, and other signal conditioning hardware. The use of EO antenna elements would roughly cut the number of required electrical channels in half if two-element phased arrays form the building blocks of a larger phased array. The challenge to using two-element phased arrays without beam steering is that they produce two possible AoA, only one of which is accurate, while phased arrays with three or more elements will yield a single accurate AoA [49]. For a three-element array to eliminate the ambiguity of the two-element array at least two of the phase differences between the three elements are needed in the DF computations [49], which would require two output channels and yield a lesser reduction in the number of channels than the two-element phased array. However, in the context of a large phased array system, additional direction estimation methods can be used to eliminate the ambiguity and determine which of the possible AoA from the two-element arrays is accurate [3]. Phased arrays of three or more EO antenna elements could be used as such an additional method of direction estimation for supplementing the two-element phased arrays. Using a small number of phased-arrays with three or more elements in conjunction with a large number two-element arrays would allow for the significant channel reduction that accompanies two-element phased arrays while eliminating the associated ambiguity in AoA.

Channel reduction promises significant savings in system hardware, especially since passive phased array radar systems can be expansive with hundreds to thousands of channels. For example, the shipboard naval radar system SPY-1 has 4100 antenna elements [50], each requiring its own channel of analog hardware to process the received signal. Even halving the number of channels leads to thousands of amplifiers, filters, and frequency converters that would no longer be necessary for the system to function with the same number of antenna elements. As such hardware is removed, savings in size, weight, cost, and power consumption are achieved. Furthermore, the reduction of channels also leads to a reduction in the amount of computing power necessary to perform the DF computations on the back end of the radar system, leading to increased efficiency in the system's digital requirements. Further study of the concept would be required, but it may also be feasible to combine the signals of additional antenna elements in higher-order MZIs, such as 4-leg MZIs, which would decrease the requisite amount of signal conditioning hardware further and lead to even greater savings of weight, space, cost, computation, and power consumption. However, the research presented in this thesis is focused on using a simple two-element phased array to provide proof-of-concept that EO antenna elements are viable for phased array radar systems.

4 Fabrication

Making EO antenna elements requires a precisely controlled microfabrication process. Furthermore, the fabricated devices must undergo a poling procedure in order to obtain a useful EO coefficient. Chapter 4 describes the fabrication and EO poling procedures performed in order to prepare EO antenna prototypes. The microfabrication process is based on the work presented in [24] and [51], as it was developed specifically for the available material set. Similarly, the EO poling procedure developed in [11] was foundational to the EO antenna elements presented in this body of work.

4.1 Fabrication Process

The structure of an EO rib waveguide is shown in Figure 4.1. Devices are built on a silicon substrate and each layer is added and processed sequentially. The bottom electrode serves as a ground plane, NOA73 polymer makes up the top and bottom cladding layers, the EO polymer SEO100C between the cladding layers serves as the waveguide core layer and the active material, and the modulating voltage is applied to the top electrode.

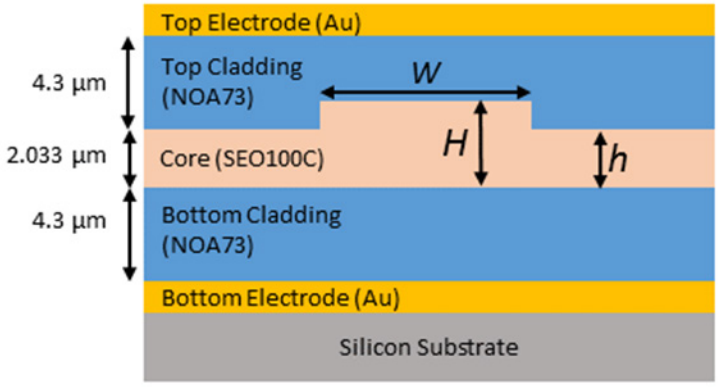

Figure 4.1 Cross-section of an EO rib waveguide showing the layer stack-up.

To form the bottom electrode, 10 nm of chrome and 100 nm of gold were deposited on a clean silicon wafer in an electron beam deposition process. The thin layer of chrome improves the adhesion of the gold to the silicon substrate. Following electrode deposition, 4.3 µm of NOA73 cladding were spin-coated on the wafer through a static spin process in which the wafer was spun at 3000 rpm for 40 seconds. It was then exposed to UV radiation in a UV box for 30 minutes to cure the NOA73 polymer.

After the deposition of the bottom cladding layer, the polymer for the EO core layer must be mixed and deposited on the wafer. The EO polymer, SEO100C, is sold in powdered form. To complete the polymer synthesis, 7.44 g of dibromomethane (CH_2Br_2) was added to 500 mg of SEO100C powder to achieve a weight percentage of 6.3% and the mixture was mixed for 8 hours at 35 rpm on a rotary mixer [35]. The SEO100C was then filtered through a 0.2 µm nylon syringe filter and allowed to settle for 30 minutes. The

SEO100C was spin-coated onto the wafer by a static spinning process. Spinning at 1000 rpm for 40 seconds produced a film 2.7 μm thick [35]. The 2.7 μm thickness was the largest thickness recommended by the manufacturer; smaller thicknesses were undesirable as they would elongate the waveguide mode shape and increase the mode mismatch between the waveguide and fiber modes. After spinning, the wafer was immediately removed to a vacuum oven where the SEO100C cured under vacuum at 75°C for at least 12 hours.

With the EO polymer in place, the waveguides were patterned in a photolithographic process. A positive resist, PR1-1000A, was employed to transfer the waveguide pattern to the EO polymer since previous studies showed it to be chemically compatible with SEO100C [24]. A 1.1 ± 0.1 μm layer of PR1-1000A was spin-coated on to the wafer and soft baked for 2 minutes at 120°C. A mask with the waveguide pattern was placed over the wafer in a mask aligner and the photoresist was exposed to UV radiation and subsequently developed with the developer RD6. The rib structure of the waveguides was etched into the SEO100C polymer by a reactive ion etch (RIE) in oxygen plasma. The average rib height of the waveguides after etching was measured with a stylus profilometer to be 667 nm. Since solvents could not be used to remove the remaining photoresist without damaging the EO core layer, the entire wafer was briefly exposed to UV light and immersed in developer a second time.

Following the etching of the SEO100C, the top cladding layer of NOA73 was spin-coated and cured with the same process described for the bottom cladding. With the core and both cladding layers in place, the wafer was baked on a hot plate covered with foil at 120°C for 2 hours to drive out any remaining solvents and improve adhesion between the polymer layers. 10 nm of chrome and 100 nm of gold were then deposited with an E-beam deposition system to form the top electrode layer. Photolithography was performed to pattern the top electrode. PR1-1000A was spun on top of the gold, a mask with the electrode pattern was aligned to the etched waveguides in a mask aligner, and the photoresist was exposed and developed. The wafer was placed first in gold etchant to remove the excess gold and then in chrome etchant to remove the underlying excess chrome.

At this point in the process, the bottom electrode is completely covered with polymer and is inaccessible. Unlike many EO antenna elements with a planar antenna electrode configuration, gaining access to the bottom electrode requires an additional RIE etch for EO antenna elements with stacked electrodes. A shadow mask of FR4 circuit board material was aligned and taped to the wafer. The wafer and mask were placed in the RIE and etched in an O_2 environment until electrical continuity was achieved between all of the bottom electrodes. This was a time-intensive etch process and required completion over a series of 10-15 minute increments to prevent the wafer from heating up and damaging the polymer layers. In between each etch, the wafer was rotated 90° to help it etch evenly. Figure 4.2 shows the prototype wafer after etching to the bottom electrode. Though not visible in Figure 4.2, radial bend waveguides are present beneath the four square patch antenna elements in a pattern similar to that shown in Figure 4.3.

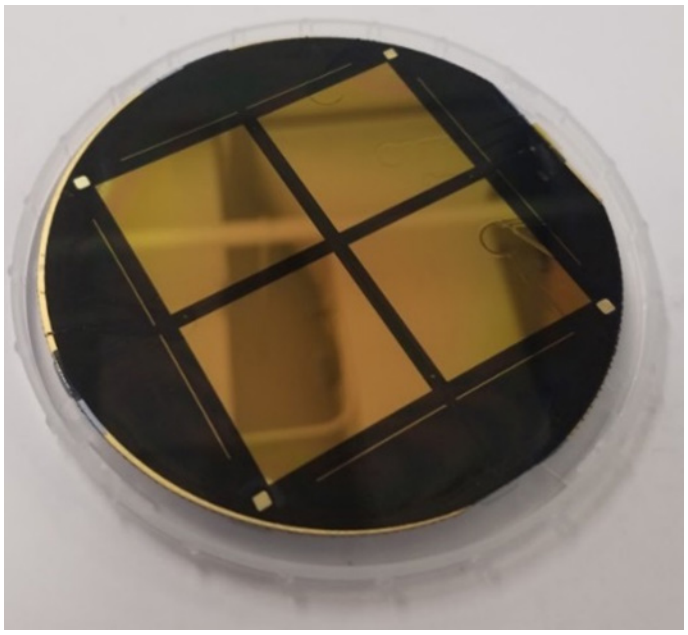

Figure 4.2 Wafer with four EO antenna elements after fabrication and prior to dicing.

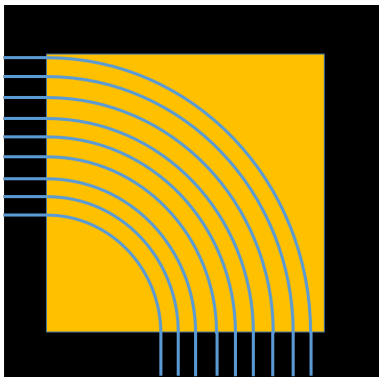

Figure 4.3 Representation of a single EO antenna element with radial bends.

Finally, a dicing saw was used to dice the wafer into individual EO devices. Each cut performed when dicing the wafer was completed in a single pass with a nickel-bonded dicing blade. The spindle speed for the blade was 30000 rpm and the cutting speed used was 40 mils/sec. Dicing is a critical step; not only is it destructive to the wafer if improperly executed, but it will determine the end face quality of the waveguides. Rough waveguide end faces will scatter light, reducing the amount of light admitted into the waveguide and increasing coupling loss. In extreme cases, rough end faces can prevent any light from coupling to the waveguide.

Careful visual inspection of waveguide end faces was performed when determining the dicing parameters to ensure the parameters used consistently produced quality end faces. Figure 4.4 shows an example of a good waveguide end face obtained from a wafer with a polycarbonate core layer that was diced with the same parameters described above. Polycarbonate is the host polymer of SEO100C and was used as a substitute core layer for

the test wafers used to determine fabrication parameters ahead of building the EO antenna elements. Polycarbonate end faces are also much easier to image with an optical microscope than SEO100C end faces.

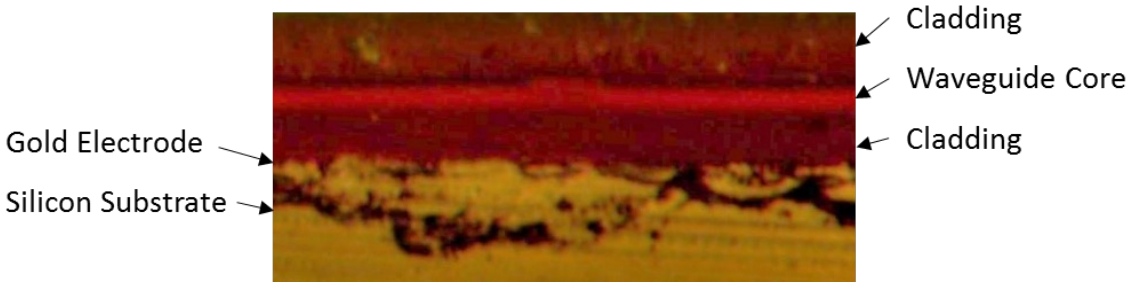

Figure 4.4 Vertical cross-section of a rib waveguide structure fabricated with a polycarbonate core layer exhibiting a cleanly diced waveguide end face.

Dicing through the entire device cross section in the manner described means that light from optical fiber must be butt-coupled into the waveguide. Butt-coupling was sufficient for testing prototype EO antenna elements. However, coupling in this fashion can increase coupling losses, particularly when permanently adhering optical fiber to the device. To better control coupling losses, future integrated EO phased array devices should utilize other coupling techniques, such as fabricated v-grooves for aligning optical fiber to the waveguides.

4.2 Electro-Optic Poling Process

The fabricated SEO100C devices were poled in a contact poling process. Contact poling, as opposed to other poling methods such as corona poling, employs a direct electrical connection between the voltage supply and the poling electrodes [38]. The devices were placed in an oven and a high voltage power supply was connected to the top and bottom electrodes by electrical probes. The oven was heated and the temperature monitored with a thermocouple. A series picoammeter simultaneously monitored the poling current. When the air temperature inside the oven reached 50°C, the power supply was turned on. The oven temperature was allowed to rise to 135°C, the glass transition temperature of SEO100C, at which point the oven was turned off [35]. After the oven cooled to 100°C, the oven door was opened to allow the device to cool more rapidly. Once the oven temperature reached 50°C, the power supply was switched off. Soluxra, the manufacturer of SEO100C recommends poling at 100 V/μm, however the voltages required to create electric fields higher than 71 V/m would cause sparking that damages the top electrodes of the fabricated devices. The devices for this body of work were therefore poled with electric fields of 62 - 71 V/μm applied across the EO polymer layer. It was observed that elevating the device being poled to allow air flow beneath the device helped the device reach the glass transition temperature more easily, producing a marked improvement in poling efficiency compared to the poling of non-elevated devices. It is

estimated that improved thermal transfer from elevating the devices yielded a 20-fold increase in the poled EO coefficient.

Figure 4.5 shows a sample plot of the measured temperature and poling current profiles. The current spike that occurs as the temperature approaches the glass transition temperature of the EO polymer is a positive indication that poling has occurred, provided that there is no dielectric breakdown [11].

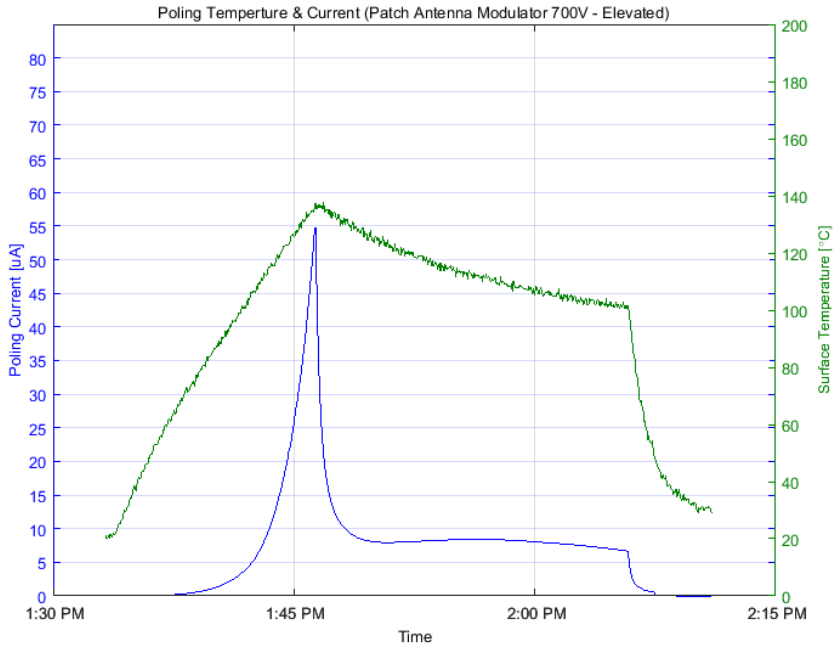

Figure 4.5 Temperature and current recorded throughout the EO poling process for a device poled at 700 V.

4.3 EO Coefficient Measurement

Following the poling procedure, the poled EO coefficient of the EO core layer was measured. This was accomplished by creating a MZI out of optical fiber, inserting an EO antenna element into the measurement leg of the interferometer, and back-calculating the EO coefficient from a measurement of the MZI half-wave voltage. When only a single EO antenna was placed in the system, direct measurement of the half-wave voltage was simple to obtain. The system diagram for this measurement is shown in Figure 4.6.

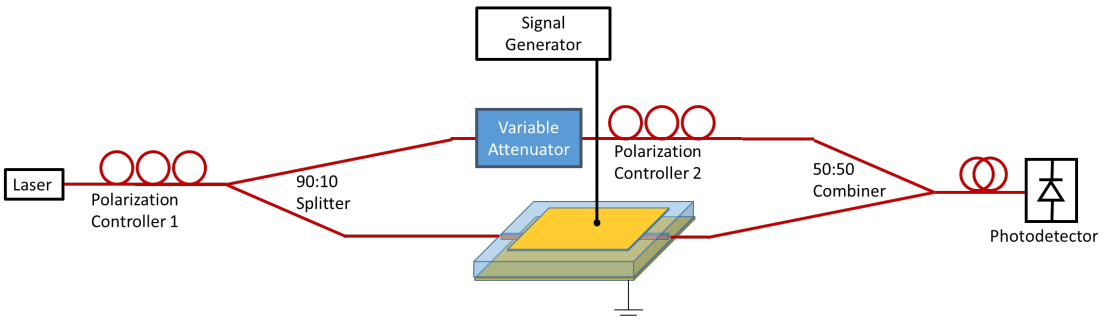

Figure 4.6 System for measuring the half-wave voltage of a single EO antenna element.

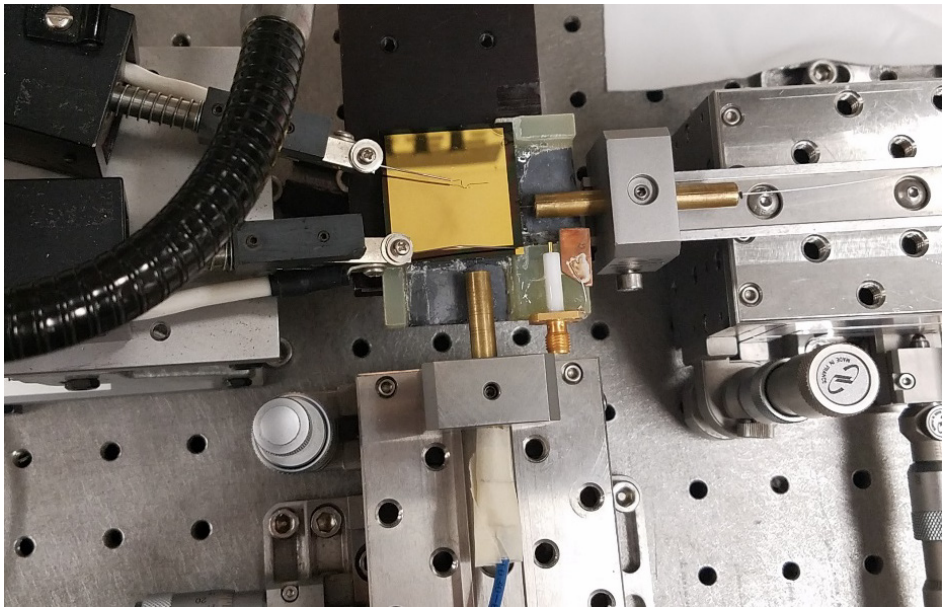

Figure 4.7 Benchtop of a single EO antenna element. Optical fiber was aligned to couple into and out of a waveguide in the device with 3-axis micrometer stages. Electrical probes make contact with the electrodes to apply the modulating voltage.

A 1545 nm laser source was used as a carrier signal and a 3-paddle polarization controller was used to ensure that TM light was sent into both legs of the MZI. Next in line, a fiber-based splitter divided the power between the two legs, sending 90% through the measurement leg (due to the high loss in the EO antenna element) and 10% through the reference leg. In the measurement leg, light was coupled through the EO antenna element and the output power was measured before the two legs were recombined. In the reference leg, a tunable attenuator was used to match the power between the two legs. Because the attenuator did not preserve the input polarization, a second polarization controller was necessary to reset the polarization to TM. Finally, a second fiber-based splitter was used to recombine the two legs and the output signal was measured with a power meter connected to an oscilloscope.

A 2 V amplitude, 1 kHz triangle wave was used to drive the EO antenna element. A triangle wave was used so that the optical response of the system could be compared and

correlated with a linear change in voltage. In the oscilloscope images, the times at which maximum and minimum power levels occur in the green output signal can clearly be distinguished. The half-wave voltage is the corresponding voltage difference in the input signal between these two times, which was measured with the oscilloscope cursors, as shown in Figure 4.8.

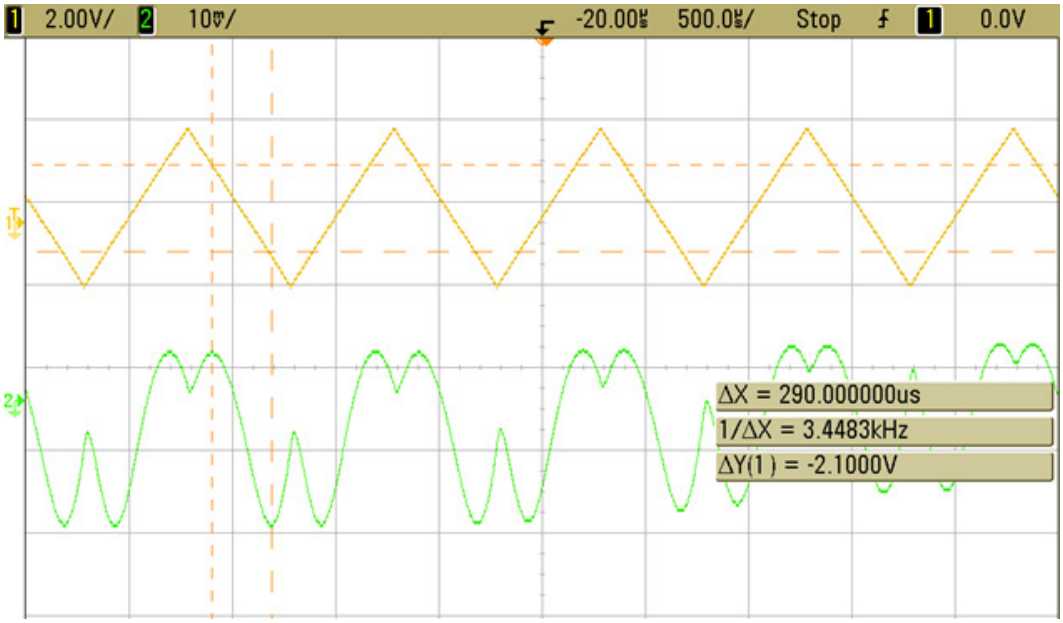

Figure 4.8 Measurement of the half-wave voltage for a single EO antenna element poled at 800 V.

If all other parameters are known, the EO coefficient (r_{33}) can be back calculated from the half-wave voltage with Equation (3.2). While the half-wave voltage measured in Figure 4.8 is 2.1 V, this value cannot be used directly to calculate r_{33} since a significant fraction of the voltage is applied over the non-active core regions. Taking into account the material resistivities and layer thicknesses, only 21% of the overall voltage (0.441 V) is applied to the core layer. In the same manner, the effective electrode separation distance is the core layer thickness (2.7 µm), not the combined polymer thicknesses (11.3 µm). The overlap integral factor from Equation (3.2) is commonly assumed to be unity for the vertically stacked electrodes that were used in this work [25, 52]. As can be seen in the simulation Figure 2.7, most of the power is confined inside the core layer. If a more precise number is required, the overlap integral can be calculated from a simulation; for these calculations, however, the overlap integral was assumed to be unity. Using these values, the core refractive index of 1.65, and the active waveguide length of 25 cm, an r_{33} of 81.2 pm/V was calculated for the device measurement shown in Figure 4.8. A second poled EO antenna element was measured in the same way to have an r_{33} of 74.08 pm/V. While the poled r_{33} values exhibit a noticeable difference between the two devices, the difference is less than 10%, pointing to a reasonable consistency in the poling process. Differences in the poled r_{33} values could have arisen from temperature variations between the two poling processes or fabrication imperfections between the devices.

5 DF Proof-of-Concept with EO Antenna Elements

The simplest possible phased array consists of two antenna elements. The spatial separation of the two antennas creates a phase difference between the signals that each antenna receives when the signals originate from a common source. From the measured phase difference and the antenna spacing, the amplitude of the received signal can be correlated to the angle of arrival (AoA).

The measurements presented in Chapter 5 demonstrate the conversion of phase modulation to amplitude modulation that would occur within a two-element EO phased array. Ultimately, the patch antennas must be able to receive radiated RF signals. By using direct injection of the electrical signals, however, the optical setup can be validated, the EO properties of the devices can be measured, and the system function can be tested without the added complexities of placing it inside an anechoic chamber and employing a transmitting antenna. The optical output signal collected from this experiment was analyzed and then compared to the theoretical radiation pattern for a two-element phased array. EO beam steering for DF with EO phased arrays is also discussed.

5.1 Mach-Zehnder System with Dual EO Antennas

To test the capacity of EO antennas for DF, a fiber-based MZI was assembled and EO antenna elements were inserted into each leg. This setup was constructed on an optical table to provide a stable base for the fiber coupling stages used to couple light in and out of the optical waveguides and a platform to build the rest of the optical system around the EO antenna elements. With two EO antenna elements in the fiber-based MZI, the fundamental operation of a two-element EO phased array was tested and the optical response to a changing phase difference recorded.

Both antenna elements were driven at the same frequency, but with a modulated electrical phase difference between them to emulate a change in AoA. Therefore, each antenna element produced a different phase delay in the optical signal. When the two optical signals were recombined, the phase difference between the antenna elements interfered to produce an amplitude modulated signal that was detected by the photodetector. Figure 5.1 shows the layout for the system used to take these measurements.

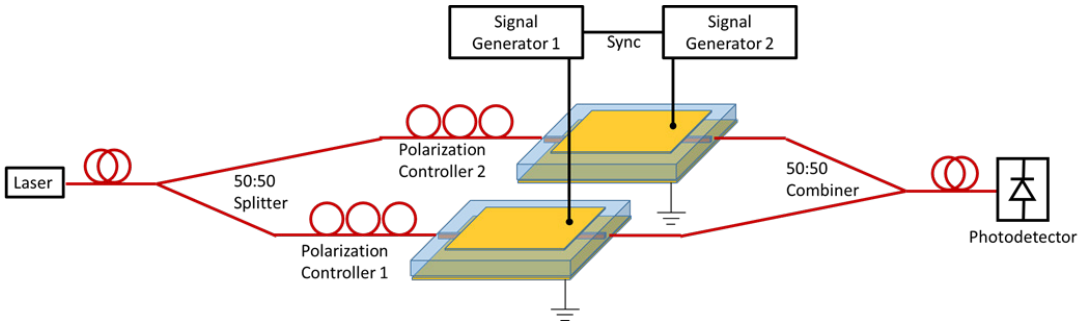

Figure 5.1 System for testing two EO antenna elements in emulation of a 2-element phased array.

Before testing the behavior of the two-element phased array system shown in Figure 5.1, a simple qualitative test was designed to show that it was able to convert a binary electrical phase difference into an intensity modulated optical signal. Two function generators were synchronized with one another to create quasi-coherent electrical signals. One function generator applied a 2 kHz, 125 mV_{pp} triangle wave, while the other used the arbitrary waveform setting to produce a binary phase shift keying (BPSK) triangle wave of the same amplitude and carrier frequency, with a phase modulation of $\pi/2$ radians at 500 Hz. The resulting input waveforms are shown in Figure 5.2.

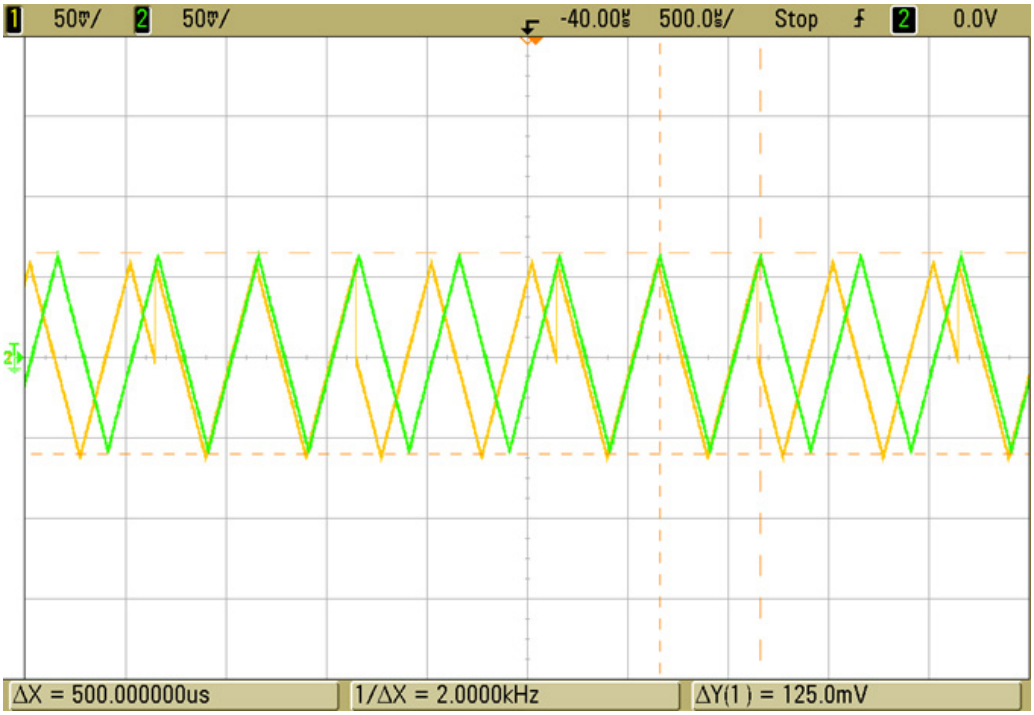

Figure 5.2 Triangle wave (green) and triangular BPSK (yellow) electrical signals applied to EO antenna elements by direct injection.

Applying these waves to the two-element phased array system should produce a signal with amplitude shift keying (ASK) modulation in a similar but simpler manner to the conversion of quadrature phase shift keying (QPSK) signals to quadrature amplitude modulation (QAM) signals described in [53, 54]. The ASK signal is expected to be a 2 kHz triangle wave with an amplitude modulation rate of 500 Hz. A power meter was the photodetector used to measure the optical output, and the resulting data confirm this result. As shown in Figure 5.3, the 2 kHz carrier signal from the input signals is preserved in the optical output and the intensity switches between two discrete levels at the 500 Hz phase modulation frequency of the BPSK input signal.

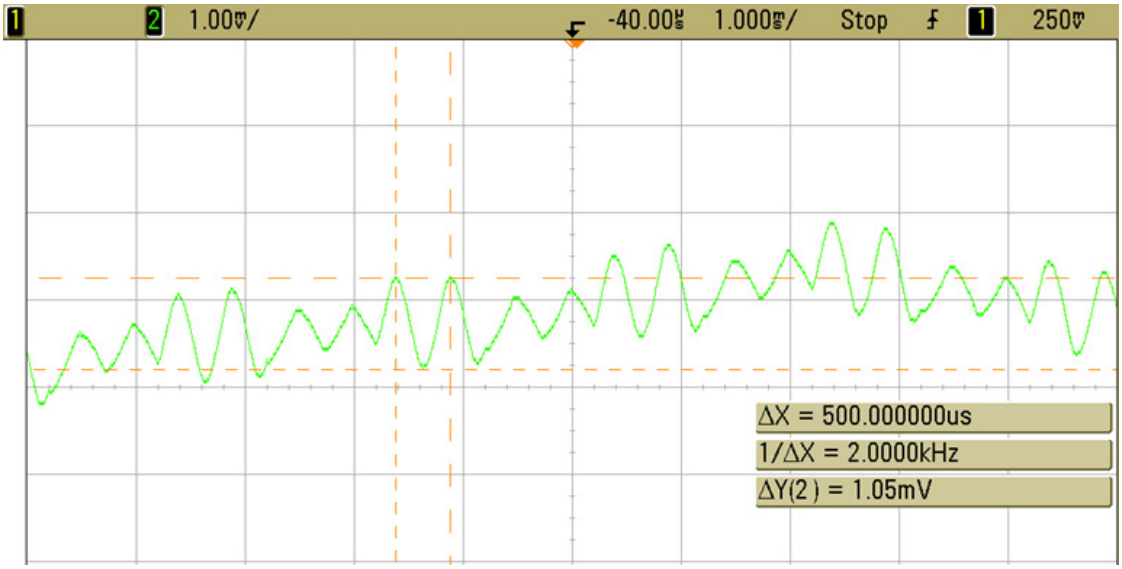

Figure 5.3 Optical output signal with triangular ASK modulation.

The BPSK modulation test provided qualitative verification that the setup behaved as expected, but was unable to further quantify the relationship between the electrical phase modulation and the optical intensity modulation because the arbitrary waveform generator used has a finite number of points defining the BPSK waveform. Despite the synchronization between the function generators, this low sample rate caused a slight phase mismatch between the two function generators that resulted in a gradual shifting of the signals in relation to one another over time.

With the fundamental functionality of the 2-element EO phased array qualitatively verified, a more sophisticated phase modulation test was designed to quantitatively relate the intensity modulation of the optical output to the phase modulation electrically applied to the antenna elements. For this test, two RF signal generators were used. The first signal generator was set to output a -10 dBm signal at 300 kHz. The second signal generator was also set to produce a -10 dBm, 300 kHz signal but with a 10 kHz phase modulation set to sweep through a total phase difference of 4π in a linear ramp function, from -2π to 2π. The electrical signals are shown in Figure 5.4; for clarity, only a portion of the 10 kHz period is shown where the phase resets from a 2π phase to a -2π phase. Additionally, when the

two signal generators were synchronized the phase mismatch seen in the BPSK modulation test between the function generators was not present.

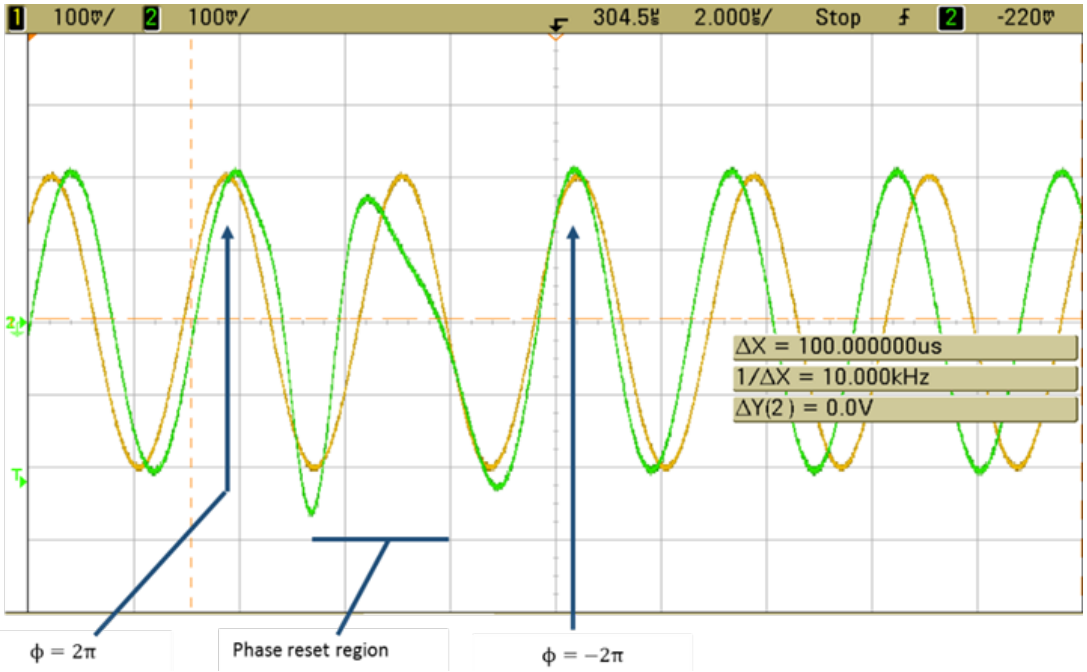

Figure 5.4 Sinusoidal 300 kHz signal (yellow) and 300 kHz signal with 10 kHz phase modulation (green) that were applied to the EO antenna elements by direct injection.

By using phase modulation in this way, a large number of electrical phase differences were applied to the system and correlated to a change in the optical output intensity. A sample of raw intensity modulation data is shown in Figure 5.5; the red arrows indicate the beginning and end of one 10 kHz period where the electrical phase difference modulated through a total phase difference of 4π. The short amplitude spikes indicated by the arrows in Figure 5.5 correspond to the distortion seen at the phase reset region of the green signal in Figure 5.4. The amplitude asymmetry in Figure 5.5 stems from the mismatch in the poled r_{33} values and EO waveguide lengths between the two EO antenna elements. With the raw intensity modulation data captured, the relationship between the output intensity modulation and input phase modulation needs to be determined and subsequently correlated to the theoretical radiation pattern for a 2-element phased array. This proof-of-concept for direction finding with EO antenna elements is addressed in Section 5.2.

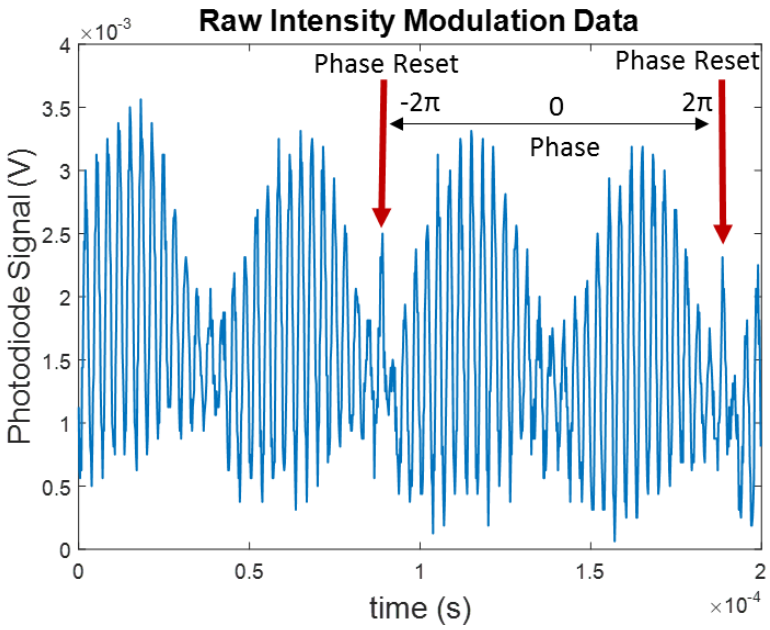

Figure 5.5 Raw intensity modulation data collected with the photodiode.

5.2 Data Analysis of Mach-Zehnder System with Dual EO Antennas

In a two-element phased array, one antenna element will be closer to the transmitter than the other, forcing the transmitted signal to travel a slightly greater distance from the transmitter to reach the second antenna. As shown in Figure 3.3, this path length difference is equal to $dcos(\theta)$ where d is the antenna spacing and θ is the AoA of the received signal [28]. The corresponding phase difference acquired over the extra distance it takes the signal to reach the second antenna is $k_{RF}dcos(\theta)$, where k_{RF} is the propagation constant for the RF signal received by the array [28]. Therefore, the slightly different path lengths that an incoming signal will take to reach each antenna create a phase difference between the two antenna elements that depends on the AoA. In the experimental setup the electrical phase difference injected to the antenna elements corresponds to this phase shift so that the phase modulation imitates a changing AoA. The electrical phase difference values over which the phase modulation occurs are known, allowing the measured amplitude from Figure 5.5 to be correlated with the electrical phase difference over one period of phase modulation from -2π to 2π radians, as shown in Figure 5.6. Since the MZI converts phase modulation in the electrical domain into intensity modulation in the optical domain, the intensity modulation of the optical signal is related to the phase difference between the antenna elements through the MZI transfer function [31]. This same principle of converting phase modulation into intensity modulation by interference is also employed by digital photonic devices such as nested MZI modulators to convert QPSK modulation from the electrical domain to QAM modulation of an optical signal [53, 54].

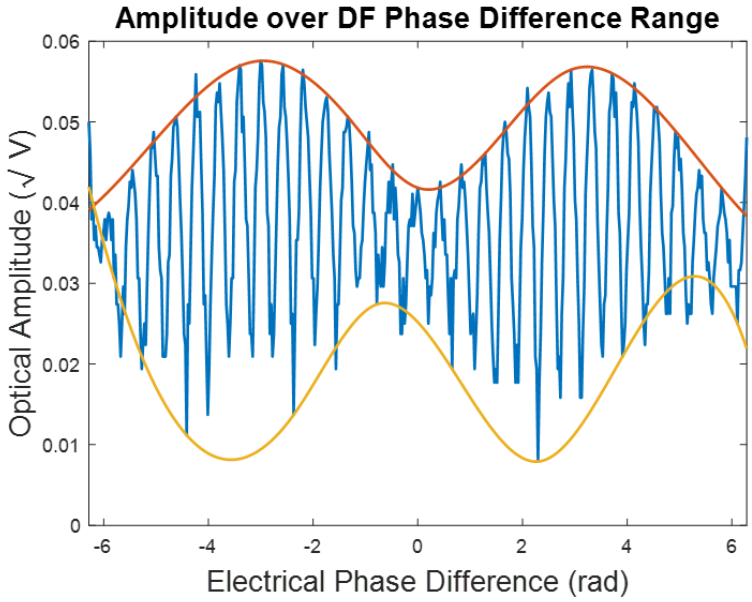

Figure 5.6 Envelope functions fit over one period of phase modulation and correlated with the electrical phase difference.

Optical sensors detect the power of the output signal, not the electric field amplitude. Therefore, the square root of the raw intensity modulation signal was taken in order for it to be proportional to the E-field amplitude resulting from the interference of the two legs of the MZI. Figure 5.6 shows one period of phase modulation with envelope functions fit to the data. From the envelope functions, the amplitude of the modulated signal was determined and related to the electrical phase difference, as shown in Figure 5.7.

To show proof-of-concept that EO antennas are suitable for DF applications, the electrical phase difference ultimately needs to be correlated to the phase difference between the signals received by two antennas, as illustrated in Figure 3.3 and mathematically expressed by Equation (5.1).

$$\phi = k_{RF} d \cos(\theta) + \beta \tag{5.1}$$

Using Equation (5.1) for a two-element phased array, the electrical phase difference (ϕ) is related to the AoA (θ), antenna spacing (d), RF propagation constant (k_{RF}), and constant phase difference (β). For an ideal two-element phased array, the antenna elements are identical and the path lengths of the MZI are equal, resulting in zero constant phase difference (β) between the antennas. In practice, however, the path lengths of the two legs may differ. Interferometers are very sensitive to path length differences. Even sub-wavelength differences in path length will significantly affect the value of β, making path length differences very difficult to estimate for fiber-based MZI used. Each EO antenna element has 25 radial bend waveguides, each of a different length, beneath the patch antenna. The two waveguides used had a length difference of 7.9 mm since, at the time of testing, two waveguides of equal length were not available on the two EO antenna

elements. Additional factors such as mismatched fiber lengths inside the MZI and air gaps between the coupling fiber and waveguide may also contribute to the value of β. The constant phase shift β in the experimental array factor must therefore be fit to the theoretical amplitude to compensate for path length differences in the experimental setup.

The theoretical array factor for a two-element phased array has a cosinusoidal dependence on the phase delay between the two antennas as noted in Equation (3.3). The amplitude in Figure 5.7 is also cosinusoidal, but is shifted phase-shifted by ~π radians. Therefore, a constant phase shift of $\beta \sim \pi$ was used to fit the experimental amplitude data to the theoretical array factor so that their peaks aligned. Since there can be no negative optical power from the system output, the amplitudes measured from direct injection of the electrical signals correspond to the absolute value of the theoretical array factor magnitude defined in Equation (3.3) that a radiated signal incident on the phased array would see.

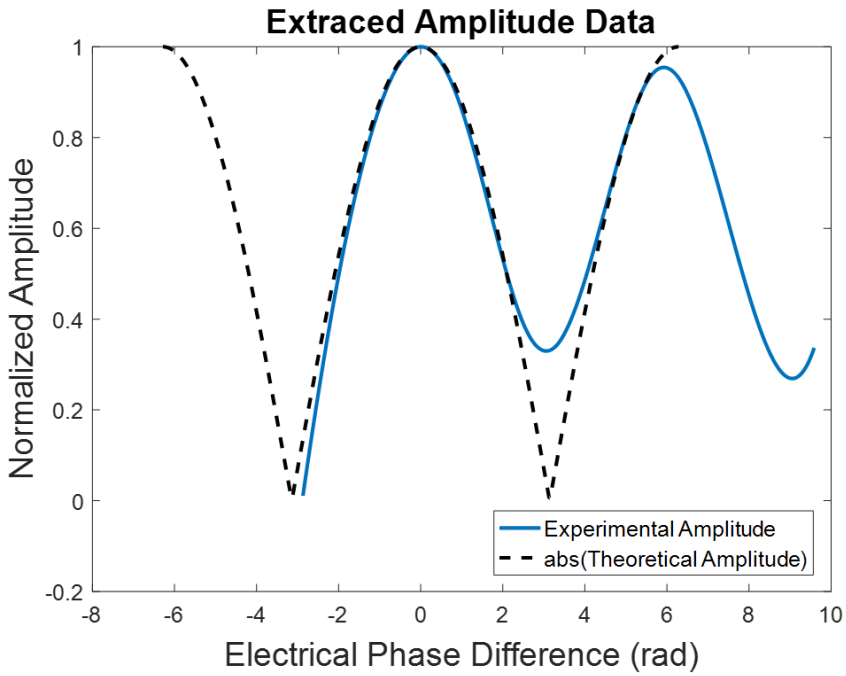

Figure 5.7 Normalized amplitude plotted against the electrical phase difference and angle of arrival. Both experimental and theoretical amplitudes are shown. A constant phase shift of β~π was applied to the theoretical data to align the peaks with the experimental amplitudes.

With all variables of Equation (3.3) known, the theoretical amplitude of the array factor can be calculated for any AoA. The AoA that correspond to the electrical phases are calculated by equating the first term of Equation (5.1) with the known electrical phase differences from the phase modulation. Because this calculation involves an inverse cosine, only a portion of the total 4π phase difference may fall within the domain of the inverse cosine function, leading to the possibility for some complex-valued angles. Figure 5.8 plots the amplitude gathered from the experimental data at each real-valued AoA and various antenna spacings (d) assuming a frequency of 300 kHz.

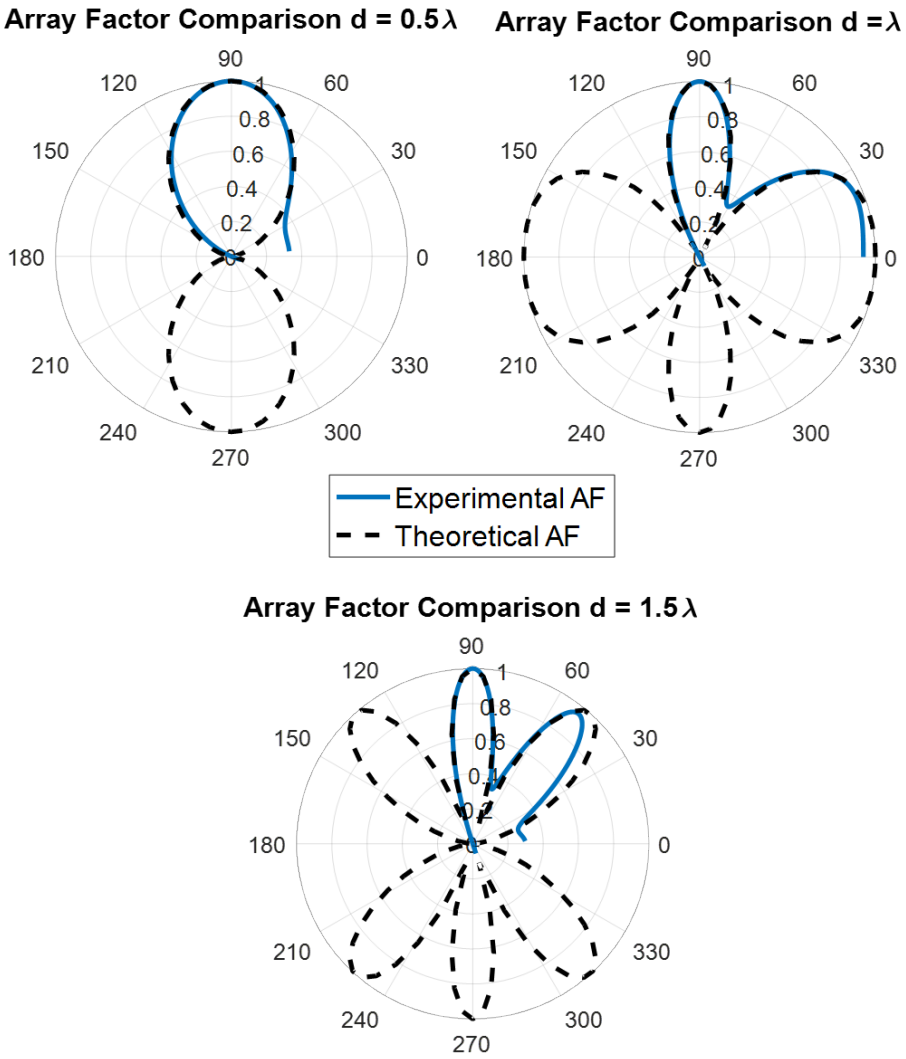

Figure 5.8 Polar plots comparing the theoretical and measured EO antenna array amplitudes and AoA for various array spacings.

In Figure 5.8 the 0.5λ antenna spacing is most practical for DF applications; however, the plots with larger antenna spacings emphasize the phased array-like behavior of the EO antenna elements. In all cases, the measured amplitudes follow with the theoretical amplitudes of the two-element array factor. The agreement between the measured and theoretical array factor patterns provides positive confirmation that EO antenna elements are suitable for phased array applications. Having shown initial proof-of-concept for the two-element EO phased array, it can be used as the fundamental building block to design increasingly more complex EO phased arrays.

It is worth noting that even for a two-element array with an antenna spacing of 0.5λ, Figure 5.8 shows that there will be ambiguity when determining the AoA since there are two AoA that correspond with each amplitude level. However, such ambiguity can be removed by adding a third antenna element to the phased array and determining the phase

difference between it and at least one of the original two antennas [1, 48, 49]. Furthermore, the precision of phased array radar increases as the number of antenna elements increases [1, 48].

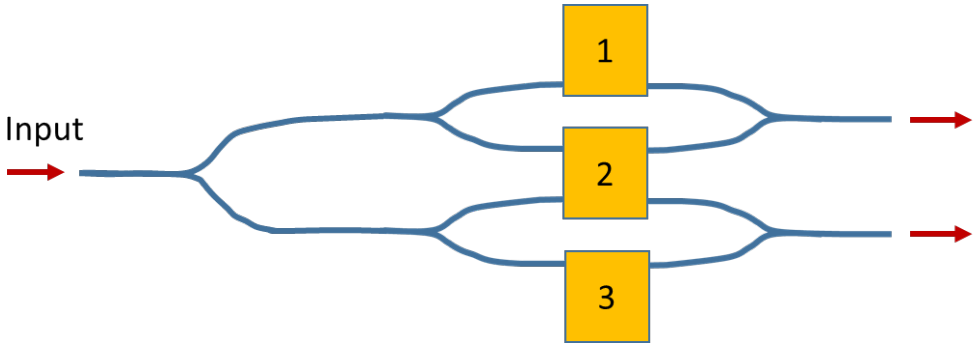

Figure 5.9 Three-element EO phased array layout. The optical outputs are proportional to the phase difference between their respective antenna elements.

Since Figure 5.8 shows that the phase difference from any two EO antenna elements in an EO phased array can be correlated to the amplitude modulation from the MZI output, the EO phased array layout from Figure 3.4 can be modified to include additional elements for future studies. One possible layout for an EO phased array with three elements is shown in Figure 5.9.

Steering the beam of the phased array is another method to reduce AoA ambiguity. By changing the phase of each antenna element in the array, the resulting interference between the radiation patterns of the antenna elements allows for angular control of the primary lobe of the array radiation pattern [55]. Electrical phased arrays employ phase shift circuitry to control the phase of each antenna channel [55], as shown in Figure 5.10. When the angular position of the radiation pattern's primary lobe coincides with the AoA of the signal received by the phased array the output signal will have its greatest amplitude. In this manner, phased arrays quickly scan all possible AoA searching for the direction of the incoming signal.

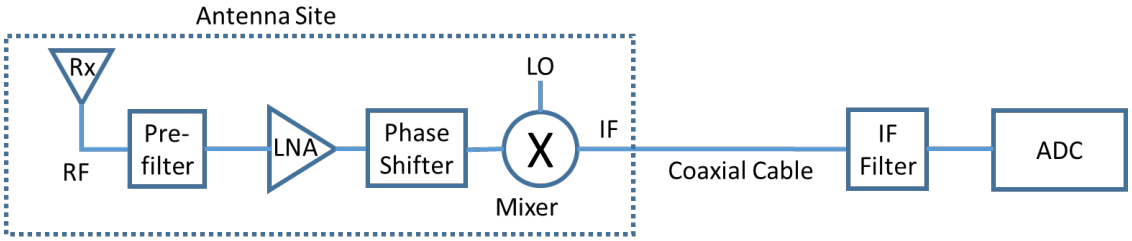

Figure 5.10 Conventional electrical channel for a passive phased array, including phase shift hardware.

In EO antenna arrays, phase control of the optical antenna signal can be achieved simply by scanning a DC voltage applied to the EO waveguide. The phase shifting capabilities of an EO antenna element are inherent to the EO effect that occurs within the waveguide material. Therefore no additional electrical phase shifting hardware is required for EO antenna arrays apart from the electrical wiring needed to apply the DC bias to the EO antenna element, allowing for hardware reduction by removing electrical phase shifters from the radar system.

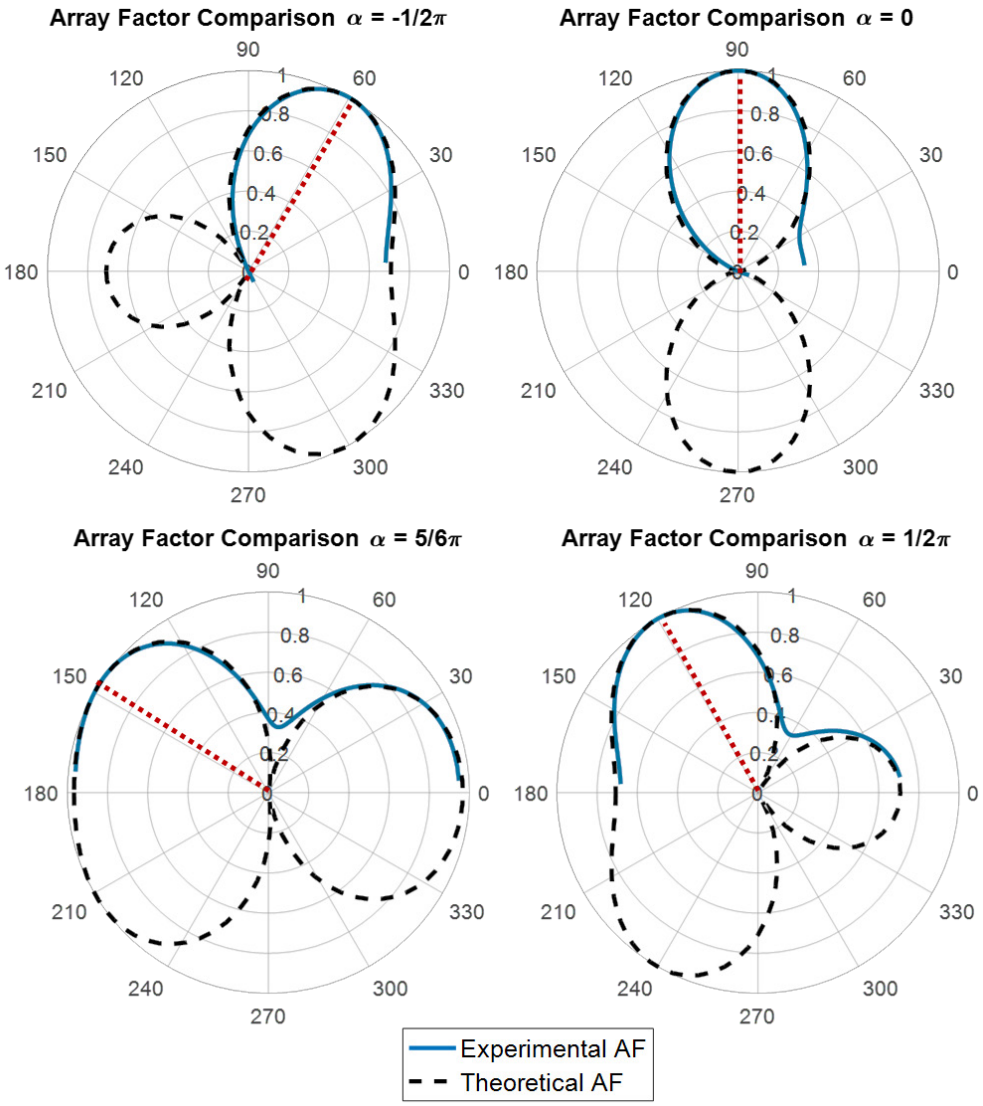

Figure 5.11 Beam steering by adding an EO phase shift (α) to a two-element phased array with a spacing $d = \frac{\lambda}{2}$.

The impact of introducing an EO phase shift for beam steering is exhibited in Figure 5.11. An EO phase shift, α, is mathematically introduced (added) to Equations (5.1) and

(3.3) to angle the primary lobe of the radiation pattern for an EO phased array of spacing $d = \frac{\lambda}{2}$. EO phase shifts of $\alpha = -\frac{\pi}{2}$, 0, $\frac{\pi}{2}$, and $\frac{5\pi}{6}$ respectively lead to primary lobe orientations of θ = 61.2°, 90°, 118.8° and 147.6°, clearly showing beam steering for the primary lobe of the two-element array.

The primary challenge to EO beam steering is that the MZI in an EO phased array must be biased with a constant phase difference of $\frac{\pi}{2}$ for linear intensity modulation. Adding a large phase difference to steer the array radiation pattern will push the MZI into a region of nonlinear operation. For example, adding a phase shift of $\alpha = \frac{\pi}{2}$ will move the MZI from its linear region to a minimum point on the MZI transfer where any modulation will be nonlinear and the output signal will be of minimal amplitude. Decreasing the spacing between antenna elements will increase the angular range for EO beam steering with associated phase shifts that keep the MZI in the linear region of its transfer function ($|\alpha| < \frac{\pi}{2}$) but will also greatly reduce the directivity of the two-element phased array. While limited EO beam steering capabilities are theoretically feasible, increasing the range of EO beam steering without degrading antenna performance deserves additional study. If effective EO beam steering is achieved with EO phased arrays, passive phased array radar systems can be simplified through the removal electrical phase shifting hardware since EO antenna elements would perform both signal reception and phase shifting functions.

6 Improvements to EO Antenna Sensitivity

Sensitivity is a key metric of EO antenna elements that has a far-reaching impact on system performance. If EO antenna elements are used to remove LNAs from the antenna site as discussed in Chapter 1, the EO antenna must be sensitive enough that moving the LNA does not impair the overall sensitivity of the receiver. Additionally, for many phased-array radar applications, it is desirable to have a long detection range. This is especially true of military applications where it is beneficial to detect and track threats that are far away, enabling military personnel have maximum time to respond to the detected threat. An improvement in the detection range of an EO antenna element corresponds to an increase in the amplitude modulation at the device output for a given incident radiated signal strength. The amplitude modulation is directly related to the magnitude of EO phase shift that occurs in an EO antenna element. Therefore, in order to increase the detection range of an EO antenna the sensitivity of the EO phase shift inside the antenna to the incident radiated E-field also needs to increase.

In this chapter, methods of optimizing EO antenna sensitivity are investigated. The resonant electric field distribution of a patch antenna is studied to determine the optimal waveguide placement for maximum EO antenna sensitivity. Furthermore, a new design that doubles EO antenna sensitivity is presented and verified through finite element analysis (FEA) simulations.

6.1 Rectangular Patch Antenna Simulation

A rectangular patch antenna with an EO core and passive cladding layers forming the dielectric was modeled in COMSOL Multiphysics 5.2a. The patch was designed to operate at 10 GHz and had the same dielectric layers as the fabricated devices from Chapter 4. In the simulation, an x-polarized 10 GHz plane wave with a strength of 1 V/m was excited in the air just above the patch surface. Figure 6.1 depicts the distribution of the resonant electric field received by the patch antenna.

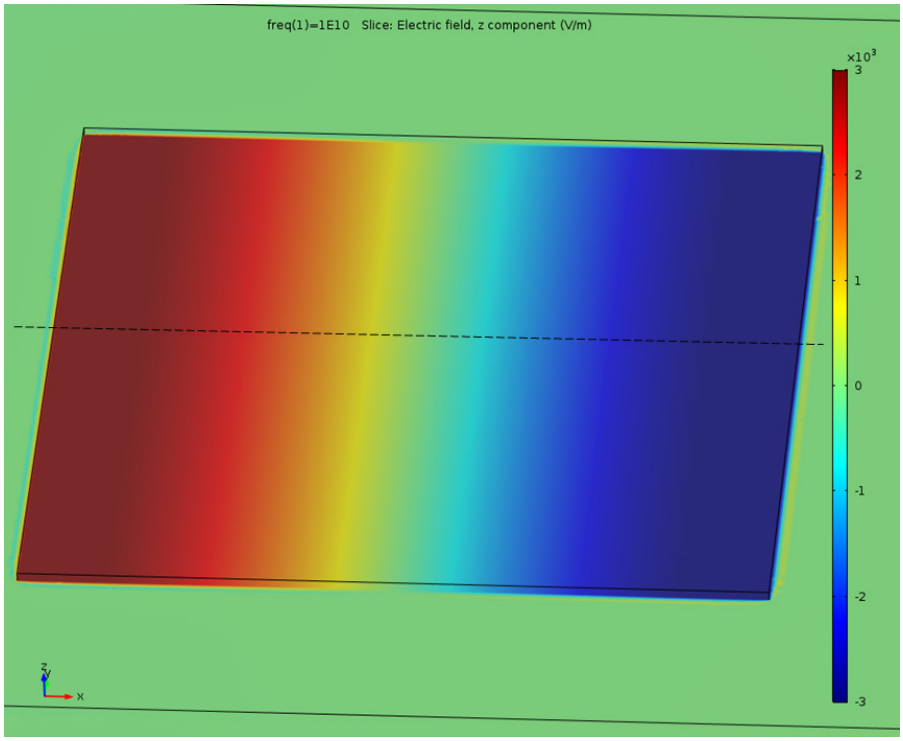

Figure 6.1 Simulated z-component of the resonant electric field for a 10 GHz rectangular patch antenna.

The simulation results agree with the theoretical E-field distribution for a resonant patch antenna described in (2.2). Figure 6.2 shows the cosinusoidal variation of the z-component of the E-field along the dashed line in Figure 6.1. In order to maximize the EO effect, the modulating E-field needs to be applied parallel to the E-field that poled the EO polymer (the z-direction, in this case). Figure 6.2 also shows that the x- and y-components of the E-field, which are indicative of any fringing fields, are much smaller than the z-component underneath the patch in the regions where the z-component of the E-field is strongest. It can be clearly seen from Figure 6.1 and Figure 6.2 that the optimal positions for waveguides in and EO patch antenna are close to the edges of the patch.

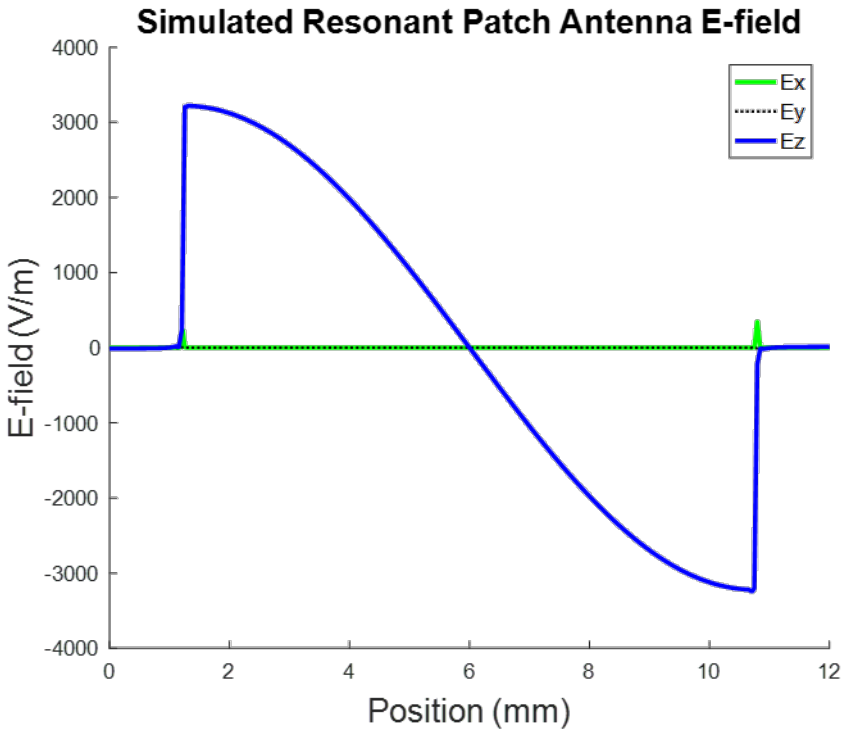

Figure 6.2 Simulated E-field components along the center line of a 10 GHz rectangular patch antenna at resonance.

6.2 Push-Pull Mach-Zehnder Driven by a Single Patch Antenna

The operational principle behind single-leg modulation of a MZI discussed in Chapter 3 can be extended to push-pull operation of a MZI, where both legs are active, but the electric fields point in opposite directions in each leg. If the applied electric fields in each leg are of equal magnitude, push-pull operation effectively doubles the sensitivity of the MZI [32].

Since the electric field on one half of a resonating patch antenna is pointed in the opposite direction of the electric field on the other end of the patch, this can be used to drive an integrated push-pull MZI interferometer directly below the patch antenna. The design is straightforward and is shown in Figure 6.3.

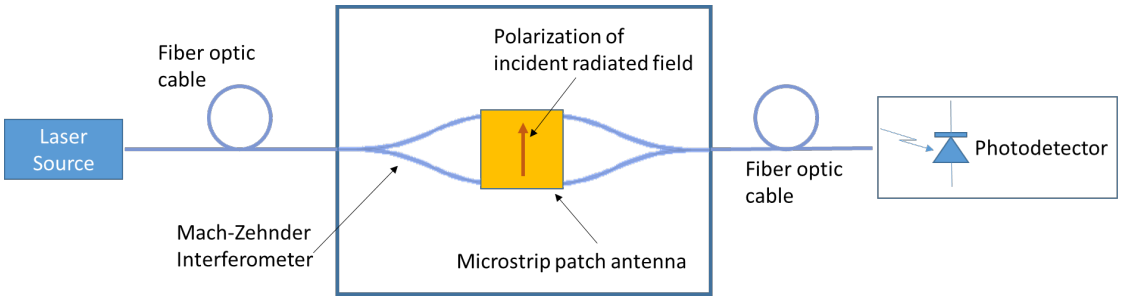

Figure 6.3 Generalized design of a push-pull Mach-Zehnder integrated with a single patch antenna.

Equation (6.1) indicates the phase shift that occurs in each waveguide. Equation (6.2) shows the total phase shift between the two legs when only one is driven by an external E-field, assuming that the active path lengths of both MZI legs are equal. If both legs of a MZI are modulated with external E-fields of the same magnitude but opposite direction, the phase difference between the two legs will double that of Equation (6.2), as shown in Equation (6.3) [25, 32]. The phase changes ($\Delta\phi$) in Equation (6.2) and Equation (6.3) are a functions of EO coefficient (r_{33}), applied electric field (E_Z), active path length (l), refractive index (n_Z), and wavelength (λ).

$$\phi = \frac{2\pi}{\lambda} n_z l - \Delta\phi \tag{6.1}$$

$$\Delta\phi_{Single\ leg} = \frac{2\pi}{\lambda}\left(\frac{{n_z}^3 r_{33} E_z}{2}\right) l \tag{6.2}$$

$$\Delta\phi_{Push-pull} = \frac{2\pi}{\lambda}({n_z}^3 r_{33} E_z)\, l \tag{6.3}$$

From the phase shift between the MZI legs, the relative amplitude of the modulated signal can be calculated with the transfer function defined from Equation (3.1). In both the push-pull and single leg modulation cases, when a modulating voltage is applied to a MZI the optical transmission will oscillate between $T\left(\frac{\pi}{2} - \Delta\phi\right)$ and $T\left(\frac{\pi}{2} + \Delta\phi\right)$ for a MZI biased at $\phi = \frac{\pi}{2}$. The output intensity over time is described in Equation (6.4), where I_{in} and I_{out} respectively represent the input and output optical power to the MZI, T is the transfer function described in Equation (3.1), $\Delta\phi$ is the respective phase difference described in Equation (6.2) or Equation (6.3), and ω_m is the angular frequency of the modulation voltage.

$$I_{out} = I_{in}\left(\left[\frac{T\left(\frac{\pi}{2}+\Delta\phi\right) - T\left(\frac{\pi}{2}-\Delta\phi\right)}{2}\right] sin(\omega_m t) + \left[\frac{T\left(\frac{\pi}{2}+\Delta\phi\right) + T\left(\frac{\pi}{2}-\Delta\phi\right)}{2}\right]\right) \tag{6.4}$$

Notably, because the phase difference for a push-pull MZI is two times greater than for a MZI with single-leg modulation, the amplitude modulation depth of the push-pull MZI will also be very close to two times greater, as shown in Figure 6.4, which plots the change in

transmission from Equation (6.4) for both the push-pull and single leg modulation phase shifts.

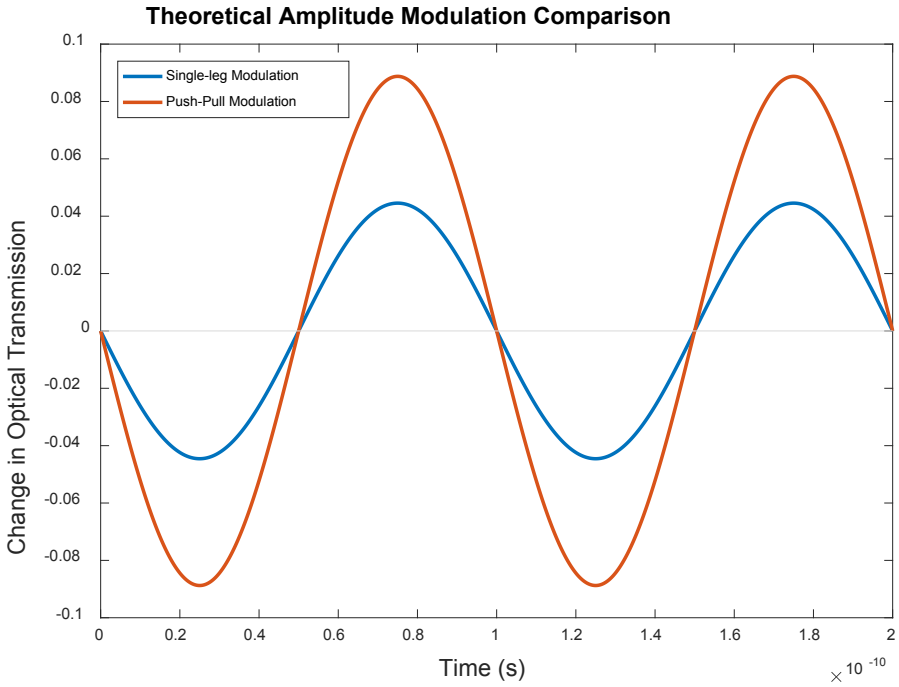

Figure 6.4 Theoretical modulation depths for a push-pull MZI and a MZI with only one leg modulated, assuming a wavelength of 1550 nm, an r_{33} of 200 pm/V, and the 10 GHz patch antenna from Figure 6.1.

6.3 Finite Element Simulation of Push-Pull Mach-Zehnder Driven by a Single Patch Antenna

A push-pull EO antenna element consisting of two EO straight waveguides driven by a single patch antenna was modeled in COMSOL Multiphysics 5.2a. The design presented utilizes the strong E-fields at the edges of the patch antenna to maximize the EO phase shift that occurs in each waveguide, while the push-pull operation doubles the sensitivity of the EO antenna compared to an EO antenna that only modulates one leg of a MZI. COMSOL's electromagnetic waves beam envelope (EWBE) physics package was used to model the optical waveguides while the electromagnetic waves (EMW) physics package was used to model the patch antenna. The simulation geometry is shown in Figure 6.5. Two parallel rib waveguides pass underneath the edges of a 100 GHz square patch antenna where the resonant electric field is strongest.

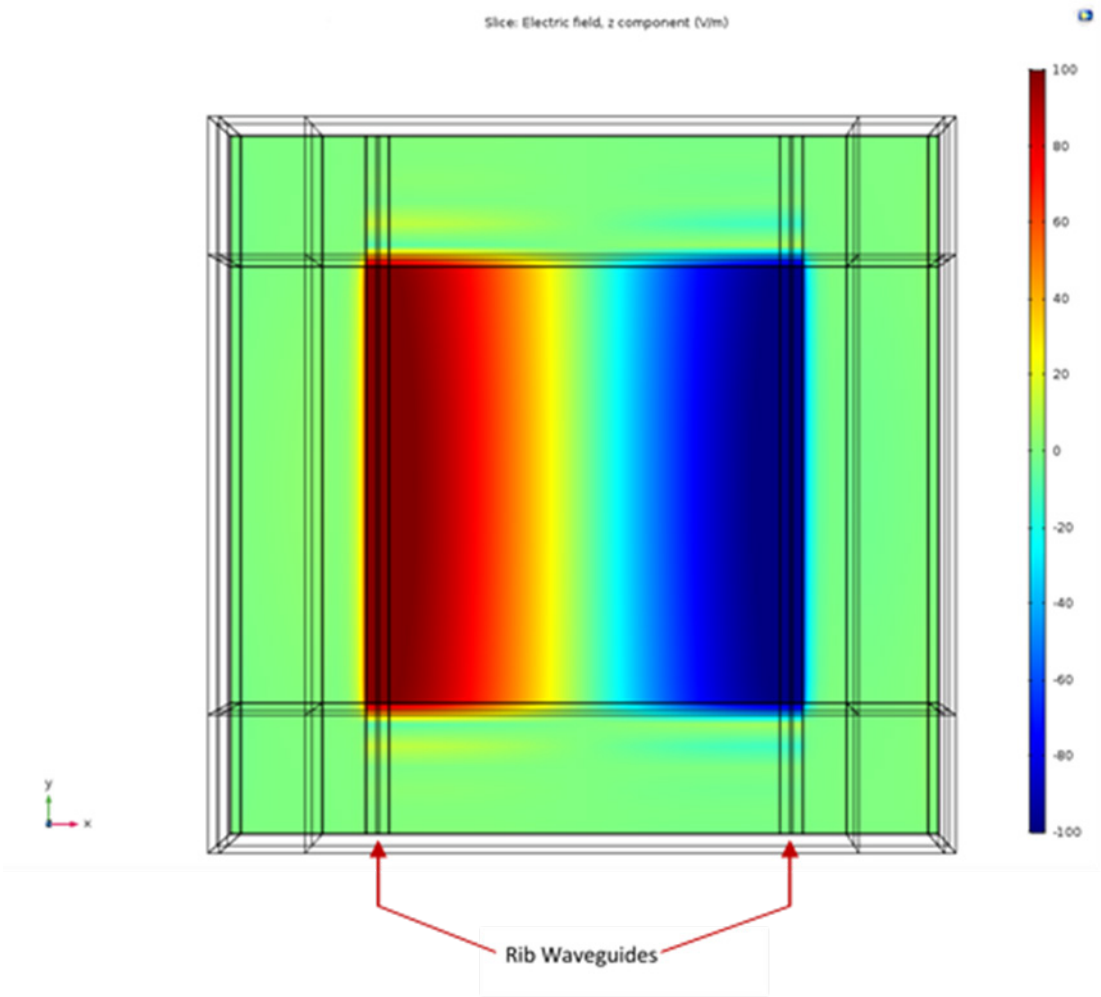

Figure 6.5 Finite element analysis (FEA) simulation of the push-pull EO antenna element showing the resonant E-field received by a 100 GHz patch antenna (top-down view).

Analogous to the fabricated waveguides presented in Chapter 4, the simulated rib waveguides were 6 μm wide with an etch depth of 667 nm and have the same refractive indices for the core and cladding layers. Coherent modes of equal optical power were computed with numeric ports and launched into the waveguides. Figure 6.6 shows the propagation of the waveguide mode through the rib waveguide.

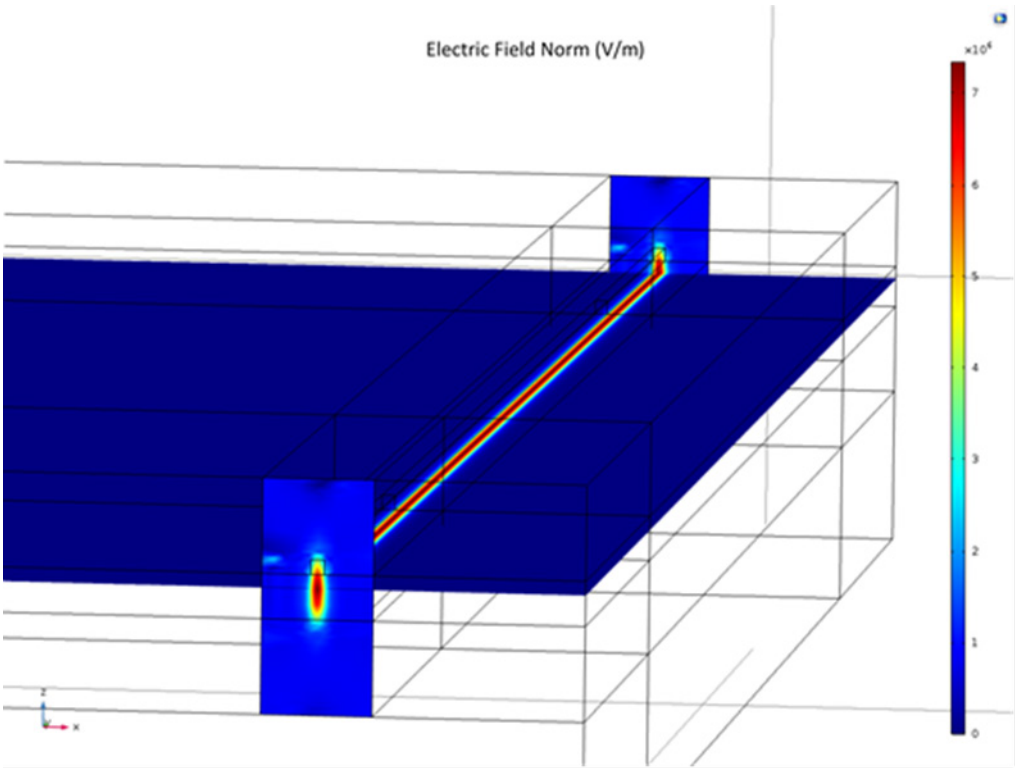

Figure 6.6 FEA simulation of optical mode propagation through an EO rib waveguide.

The phase was determined along the length of each waveguide in order to calculate the resulting amplitude modulation in the post-processing of the simulation results. Instead of modeling the Y-splitter used to recombine signals in an integrated MZI, the amplitude modulation was calculated from the phase difference between the waveguide outputs using Equation (6.4) with the respective phase difference for single-leg or push-pull modulation of a MZI . Y-splitters were not included in the model geometry because, when meshing in three dimensions, the swept mesh needed for mode propagation with COMSOL's EWBE physics would not follow both legs of the Y-splitter. Using tetrahedral mesh elements and EMW physics may adequately model the Y-branch in three dimensions. However, in comparison to EWBE physics, there would be a substantial increase in the computational resources required. The EMW physics package requires several mesh elements per wavelength to properly resolve the E-field propagation, while the slowly-varying envelope assumption in the EWBE physics is not constrained in this manner and can model the E-field propagation with far fewer mesh elements [56].

The EMW physics package was used to simulate the patch antenna. The perfect electric conducting boundary condition was used to model the patch antenna and ground planes. An x-polarized plane-wave RF signal with a field strength of 1 V/m was excited in the air directly above the patch antenna. The patch antenna was designed to resonate at 100 GHz in order keep the physical dimensions of the simulation small and minimize the computational load of the simulation. The resulting patch dimensions of the square 100 GHz patch are 0.949 mm.

The resonant E-field in the vertical direction shown in Figure 6.5 was used to calculate the index of refraction change of the EO core material using Equation (2.4) within the simulation and the optical mode propagation was simulated. The refractive indices of the simulated core and cladding layers under zero bias were 1.65 and 1.56, respectively. Furthermore, the core and cladding layers were assumed to have zero conductivity. A high r_{33} value of 200 pm/V was chosen to ensure that an observable phase shift was present despite the short active length (~1 mm) of the 100 GHz patch antenna. EO coefficients around 200 pm/V have been measured in thin films of the EO polymer SEO100 [12]. Table 6.1 summarizes the FEA simulation parameters while Figure 6.7 shows the relative positions and magnitudes of the RF and optical E-fields in the region of one of the waveguides.

Table 6.1 Summary of parameters used in COMSOL FEA simulation

Simulation Parameter	**Value**
Optical Wavelength	1550 nm
RF Frequency	100 GHz
RF Field Strength at Antenna	1 V/m
Patch Dimension	0.949 mm
Waveguide Width	6 μm
Rib Height	667 nm
Waveguide inset from patch antenna edge	25 μm
Core Refractive Index	1.65
Core Thickness	2.7 μm
Cladding Refractive Index	1.56
Cladding Thickness	4.3 μm
Core Layer EO Coefficient	200 pm/V

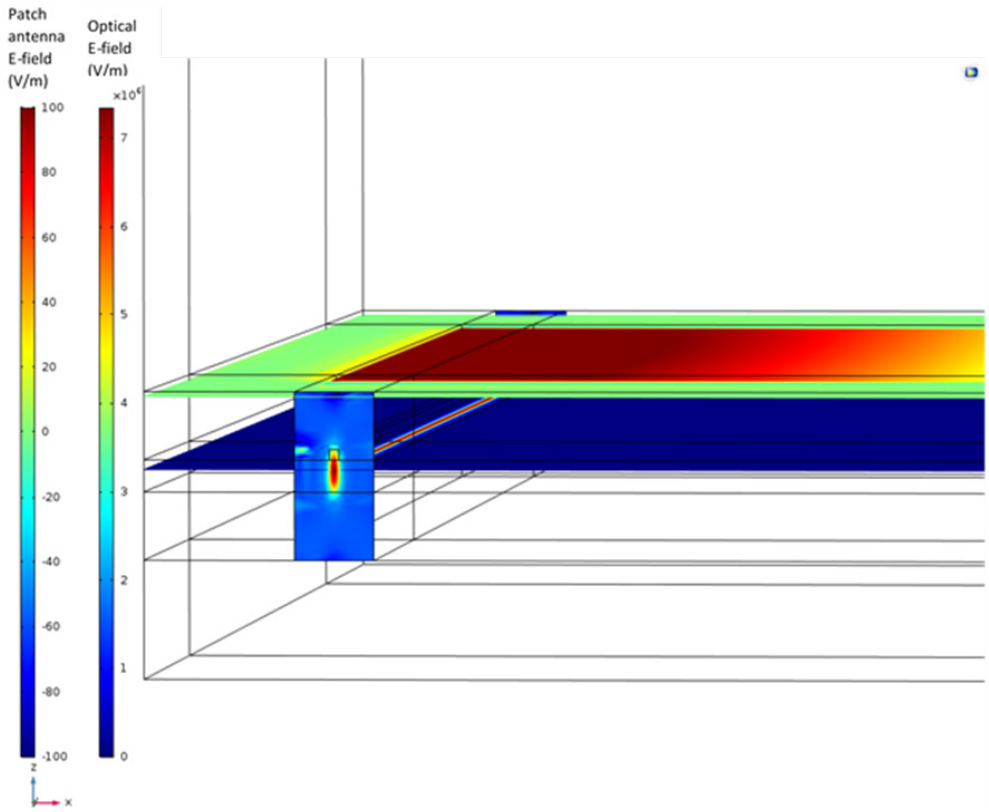

Figure 6.7 Superposition of the RF and optical electric fields in the region surrounding one waveguide.

One-dimensional cut lines were defined along the center of each optical mode. The optical phase was found along each of these lines by computing the inverse tangent of the ratio of the imaginary component of the optical field in the z-direction to the real component of the optical field in the z-direction. The phase data from each waveguide were exported in order to be processed outside of COMSOL and were subsequently imported into MATLAB where the phase difference between the waveguides was computed. The raw phase difference data has some inherent noise as seen in Figure 6.8, but it does exhibit the sloped phase expected along the patch antenna region where the external E-field is applied.

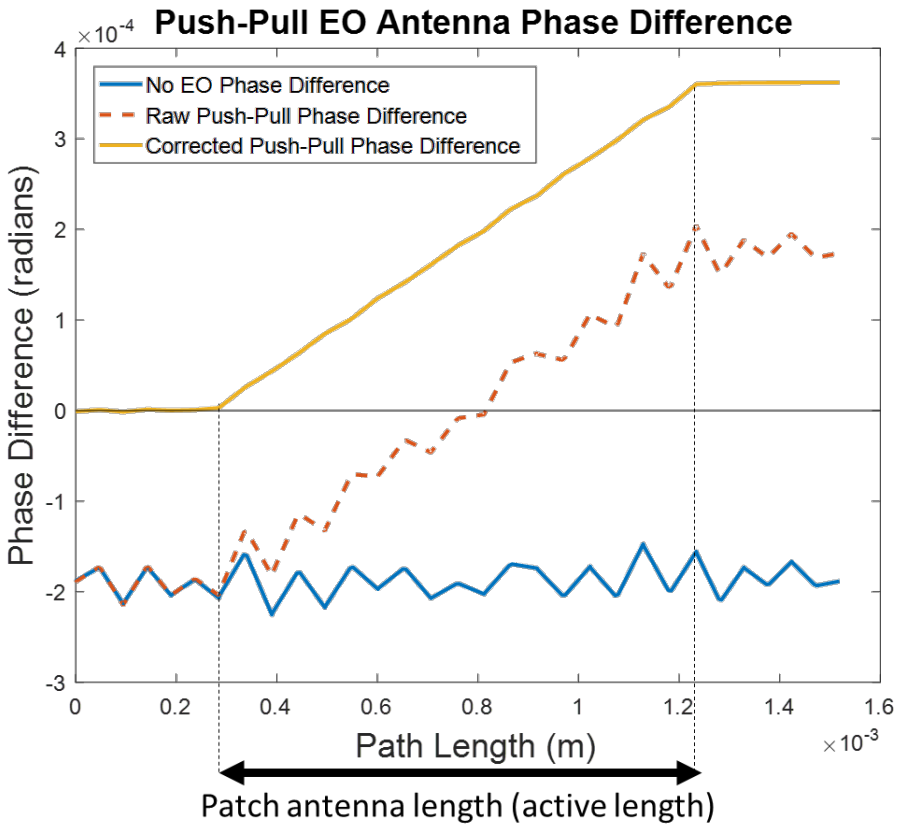

Figure 6.8 Push-pull EO patch antenna phase differences.

The phase difference error is due to the inherent discretization of the finite element simulation. By increasing the mesh resolution in the waveguide cross-section, the phase difference error decreases. However, improving the mesh resolution at the waveguide cross-section only achieves a slight improvement in phase difference at significant computational expense. The phase difference error does not depend on the applied electric field and can be corrected for by simulating the optical propagation without the external E-field. The phases along waveguides with no EO effect are subtracted from one another to determine the phase difference error. This error can then be subtracted from the raw phase difference of the EO simulation. As shown in Figure 6.8, the result is a much smoother corrected phase difference that begins at zero, increases linearly across the patch length where the external E-field is applied and then maintains a constant phase difference past the patch antenna.

Running the simulation with no EO effect was further useful in that the push-pull operation from the patch antenna can be compared with the modulation of a single leg of an integrated Mach-Zehnder. The phase of a waveguide from the simulation with the resonant E-field from the patch antenna can be subtracted from the phase of the corresponding waveguide without the applied E-field. This can be done for the waveguide with the positive external E-field, as well as the negative external E-field. It can be shown from Equation (6.3) and Equation (6.1) that a negative phase shift is produced in the

waveguide when the optical and RF fields align with one another and a positive phase shift is produced when the two E-fields oppose one another. For the FEA simulation, the optical E-field points in the negative z-direction. The results shown in Figure 6.9 therefore agree with the theoretical EO phase shift: the positive applied E-field produces a positive phase shift while the negative applied E-field produces a negative phase shift. Furthermore, Figure 6.9 shows that the simulated phase difference for single-leg modulation of Mach-Zehnder is half of the push-pull difference. These phase differences can be input into Equation (6.4) to determine the amplitude modulation resulting from the interference between the two Mach-Zehnder legs. Figure 6.10 also shows that the push-pull EO patch antenna doubles the amplitude modulation of the output signal compared to an EO patch antenna with single-leg modulation of the Mach-Zehnder.

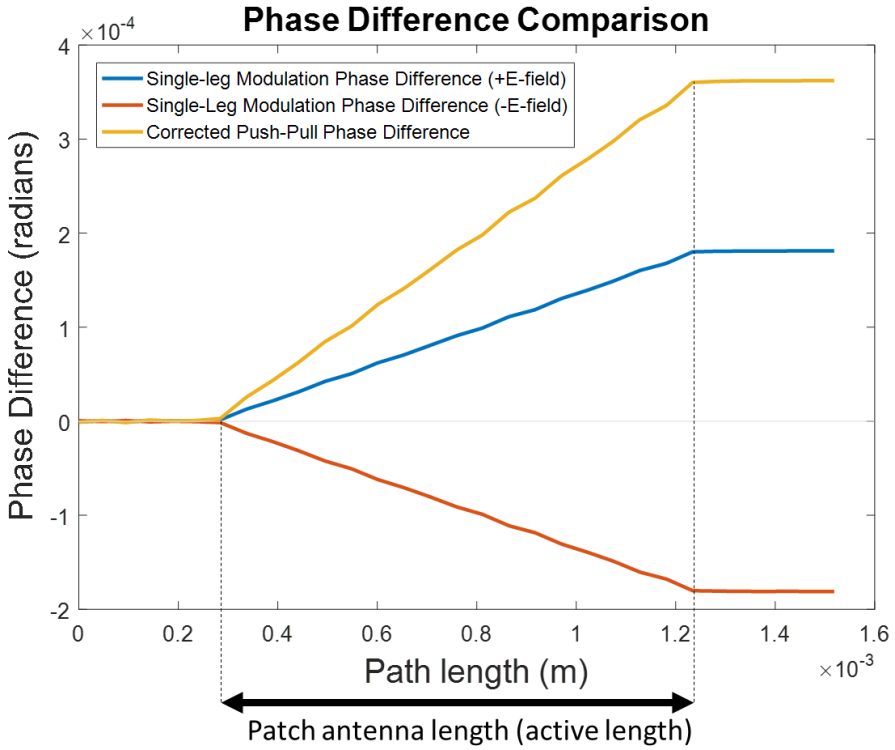

Figure 6.9 Phase shift comparison between an EO patch antenna with a push-pull Mach-Zehnder and EO patch antennas with single-leg modulation of the Mach-Zehnder (positive and negative voltage cases).

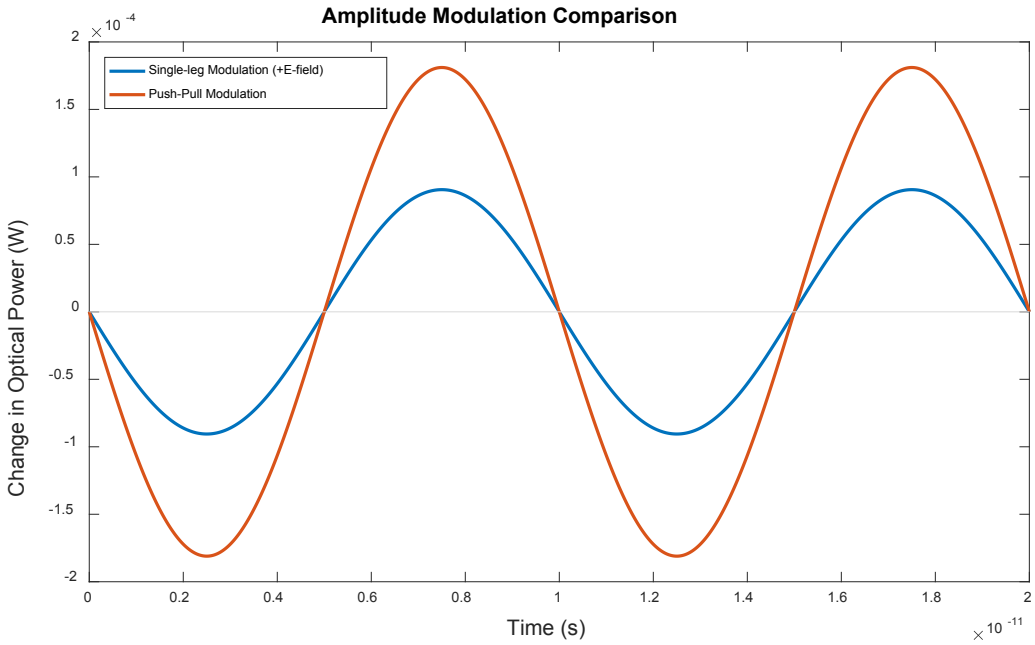

Figure 6.10 Comparison of the amplitude modulation resulting from the single-leg modulation and push-pull modulation phase shifts assuming 1 W of input power and lossless waveguides.

The design presented here could be modified to further increase the sensitivity of an EO patch antenna by passing the waveguides underneath the patch antenna multiple times so that each leg of the MZI acquires additional phase shifts. Push-pull modulators have been designed so that each leg of the MZI passes underneath its respective electrode twice, resulting in an increased EO phase shift [52]. However, due to the sinusoidal E-field distribution across a resonant patch antenna, each additional pass of an EO waveguide beneath would yield diminishing increases in phase shift as the waveguides approach the center of the patch where the resonant E-field magnitude goes to zero. Furthermore, each additional pass beneath a patch antenna will add additional waveguide loss to the antenna element as the waveguide path length becomes longer. In the context of an array of EO patch antennas fabricated on a single substrate, managing the waveguide loss becomes an important concern since extreme attenuation of the optical signal strength would make the output more difficult to detect and could thereby impair the performance of the EO antenna array.

7 Conclusion and Future Work

7.1 Conclusion

EO antenna elements receive radiated signals and modulate them into the optical domain without additional hardware, allowing for low-loss transmission of RF signals over optical fiber. In this way, EO antenna elements have a distinct advantage over their conventional electrical counterparts since EO antenna elements do not require any electrical hardware between the antenna and the optical fiber. The work detailed here presents EO antenna elements as an emergent technology that is viable for application in passive phased-array radar systems. Prototype EO antenna elements were fabricated and their passive and active behaviors were characterized. Additionally, a novel push-pull EO patch antenna design that improves EO antenna sensitivity was developed and simulated.

EO patch antenna elements were fabricated, the single mode behavior of the waveguides was verified, the refractive index of unpoled SEO100C was measured to be 1.655, and the waveguide loss was measured through the cutback method to be 4.2 dB/cm. A triangle-wave modulation voltage was introduced via direct injection to a single EO antenna within a fiber-based MZI to measure V_π. This measurement was performed on two separate EO antenna elements and the EO coefficients of 81.2 and 74.08 pm/V were back-calculated. The active behavior of both devices was further tested by placing one EO antenna in each leg of the fiber-based MZI and modulating both devices simultaneously. Electrical signals were directly injected to the EO antenna elements and the phase difference between the two elements was swept. The optical output was then correlated to the theoretical array factor for a two-element phased array, showing the suitability of EO antenna elements for use in phased array applications. Additionally, it was mathematically demonstrated how sweeping a DC bias on EO antenna elements in a phased array could be used for beam steering.

The resonant E-field distribution across a rectangular patch antenna was simulated with FEA in order to optimize the sensitivity of EO antenna elements. A patch antenna's resonant E-field has parallel regions with field vectors that point in opposing directions. Such an E-field distribution naturally lends itself to driving push-pull operation in a MZI. Further FEA simulations were performed to show proof-of-concept that driving a MZI in push-pull operation from a single patch antenna doubles the EO antenna sensitivity compared to an EO antenna that modulates one leg of a MZI.

7.2 Future Work

There are many improvements to the fabricated devices that can be addressed in a second generation of EO antenna elements. The fiber-based MZI used in the active characterization of the prototype EO antennas worked well for gathering the initial measurements presented in this work, but needs improvement for further progress to be made. Most notably, a low-frequency instability was observed in the optical output of the

signal. The data collected for this work bypassed this instability by modulating at frequencies that were much higher than the noise, but such noise must be eliminated prior to any real-world implementation of EO phased arrays. The most likely cause of the instability is the fact that the butt-coupling of optical fiber to the waveguide end face occurs within the MZI legs. This means that any displacements due to environmental vibrations, even small sub-micron displacements, can introduce significant phase noise between the two legs. Such phase noise would then translate to amplitude variations in the optical output signal. Two improvements could address this issue. The first improvement involves designing a method of permanently coupling and fixing input and output fibers to the device, which is already necessary prior to implementing this technology in radar systems. One common method for doing this is by making v-groove trenches leading up to the waveguide where bare optical fiber can be placed in a coupled position to the waveguide and then glued in place. The second and more controllable way to remove the possibility of phase variations due to fiber position drift inside the MZI is to fabricate devices where the MZI is integrated beneath the patch antenna array. With an integrated MZI the splitting, path lengths, and recombination of the legs are fixed and the phase difference between the legs is more controlled.

While the EO antenna elements tested in this work were designed to operate in the S-band, there are no factors inhibiting future designs from being scaled to operate in the X-band, a more common frequency band for radar systems. Such scaling would see additional benefits including higher device yield per fabricated wafer, smaller device size, and lower optical loss. At the time of writing, X-band EO antenna arrays with integrated Mach-Zehnders have been fabricated, but still require significant testing.

One notable challenge to integrated EO phased arrays is high waveguide loss. The 4.2 dB/cm loss measured for the waveguides fabricated with the NOA73 and SEO100C material set restricts the practical size and complexity of integrated EO phased arrays made with this EO polymer. SEO100C is has a high EO coefficient, but the waveguide loss measured here is roughly double that of similar waveguides made with DR1, an EO polymer with a much lower r_{33} value [42, 52]. Since the active region of most EO waveguide devices is usually smaller than the overall waveguide length, there is no need to propagate light through EO polymer in the non-active regions of a device. Adiabatic taper designs have been developed to integrate EO polymer waveguides with passive waveguide materials [57]. Such designs show promise to retain the benefits of a high EO coefficient while mitigating the higher waveguide loss native to these materials by introducing lower loss passive materials for the non-active device lengths.

Since all active testing presented in this work was done by injecting the electrical signal directly onto the patch antenna, the next step for the two-element array presented herein involves testing the system under direct radiation from an RF source in an anechoic chamber. By rotating an EO phased array inside an anechoic chamber, the array response to a changing AoA can be measured. Anechoic chamber testing can also determine the minimum signal strength that EO antenna elements are able detect, setting a benchmark for designing the sensitivity of future EO antennas. While initial sensitivity measurements for

EO bowtie antenna elements [15, 58], EO patch antennas [19, 22], and EO tapered dipole antennas [20] have been made, most of these have used planar antenna electrodes with TE waveguides. To the author's knowledge no sensitivity measurements of stacked antenna electrodes and TM waveguides made from EO polymer material have been made as of this writing.

Finally, a push-pull MZI driven by a single patch antenna needs to be tested to fully validate the simulation results presented in this work. The test of this design should include radiating a push-pull EO patch antenna and an EO patch antenna that drives one MZI leg at the same RF frequency and signal strength. The expected result is that the amplitude modulation of the push-pull EO patch antenna would be twice that of its counterpart that only modulates one leg of its MZI. As with the integrated EO patch antenna array, EO patch antennas with a push-pull MZI have been fabricated but still require testing. The push-pull EO patch antenna could also be further developed by passing waveguides beneath the patch antenna multiple times to maximize the EO phase shift acquired by the optical signal.

8 Reference List

[1] "Introduction into Theory of Direction Finding," in *Radiomointoring & Radiolocation,* Rohde&Schwarz,ed.: Rohde & Schwarz, 2010, pp. 26-49.

[2] S. Tokoro, K. Kuroda, A. Kawakubo, K. Fujita, and H. Fujinami, "Electronically scanned millimeter-wave radar for pre-crash safety and adaptive cruise control system," in *IEEE IV2003 Intelligent Vehicles Symposium. Proceedings (Cat. No.03TH8683)*, 2003, pp. 304-309.

[3] P. Q. C. Ly, "Fast and Unambiguous Direction Finding for Digital Radar Intercept Receivers," PhD, Electrical and Electronic Engineering, University of Adelaide, 2013.

[4] S. Babani, A. A. Bature, M. I. Faruk, and N. K. Dankadai, "Comparative Studey Between Fiber Optic and Copper in Communication Link," 2014.

[5] F. Chastellain, C. Botteron, E. Firouzi, P.-A. Farine, P. Weber, and J.-P. Aubry, "A Dual-Frequency RF Front-End for Long Antenna-GPS Receiver Links," in *Proceedings of the 18th International Technical Meeting of the Satellite Division of The Institute of Navigation (ION GNSS 2005)*, Long Beach, CA, 2005, pp. 1720-1727.

[6] RF Industries, "50 Ohm Low Loss, High Performance Coaxial Cable," CBL-CU195,

[7] C. H. Cox III and E. I. Ackerman, "Fiber-Optic Analog Radio Frequency Links," in *Broadband Optical Modulators*: CRC Press, 2016, pp. 82-111.

[8] Corning, "SMF-28 Ultra Optical Fiber," SMF-28, 2014.

[9] X. S. Yao, G. Lutes, R. T. Logan, Jr., and L. Maleki, "Field demonstration of X-band photonic antenna remoting in the Deep Space Network," *The Telecommunications and Data Acquisition Report,* pp. p 29-34, 1994.

[10] J. Manjula and A. R. Bevi, "A 79GHz Adaptive Gain Low Noise Amplifier for Radar Receivers," *International Journal of Engineering & Technology,* vol. 7, no. 2.24, 2018.

[11] M. J. Briseno, "Electro-Optic Contact Poling of Polymer Waveguide Devices and Thin Films," M.S., Michigan Technological University, Ann Arbor, 10617020, 2017.

[12] Y. Jouane, Y. C. Chang, D. Zhang, J. Luo, A. K. Jen, and Y. Enami, "Unprecedented highest electro-optic coefficient of 226 pm/V for electro-optic

polymer/TiO(2) multilayer slot waveguide modulators," *Opt Express,* vol. 22, no. 22, pp. 27725-32, Nov 3 2014.

[13] X. Zhang *et al.*, "Antenna-coupled silicon-organic hybrid integrated photonic crystal modulator for broadband electromagnetic wave detection," *Journal of Lightwave Technology,* vol. 32, no. 20, pp. 3774-3784, 2015.

[14] R. Hill, "A Practical Guide to the Design of Microstrip Antenna Arrays," *Microwave Journal,* Available: https://www.microwavejournal.com/articles/3144-a-practical-guide-to-the-designof-microstrip-antenna-arrays

[15] O. D. Herrera *et al.*, "Silica/Electro-Optic Polymer Optical Modulator With Integrated Antenna for Microwave Receiving," *Journal of Lightwave Technology,* vol. 32, no. 20, pp. 3861-3867, 2014.

[16] Y. Xiao, M. Hofmann, Z. Wang, S. Sherman, and H. Zappe, "Design of all-polymer asymmetric Mach-Zehnder interferometer sensors," *Applied Optics,* vol. 55, no. 13, pp. 3566-3573, 2016/05/01 2016.

[17] C. H. Bulmer, W. K. Burns, and R. P. Moeller, "Linear interferometric waveguide modulator for electromagnetic-field detection," *Optics Letters,* vol. 5, no. 5, pp. 176-178, 1980/05/01 1980.

[18] H. Murata, N. Suda, and Y. Okamura, "Electro-optic modulator using patch antenna-coupled resonant electrodes and polarization-reversed structure for radio-on-fiber systems," in *2009 Conference on Lasers and Electro-Optics and 2009 Conference on Quantum electronics and Laser Science Conference*, 2009, pp. 1-2.

[19] D. H. Park, V. R. Pagán, T. E. Murphy, J. Luo, A. K. Jen, and W. N. Herman, "Free space millimeter wave-coupled electro-optic high speed phase modulator based on nonlinear optical polymer in-plane waveguide structure," in *2014 Conference on Lasers and Electro-Optics (CLEO) - Laser Science to Photonic Applications*, 2014, pp. 1-2.

[20] B. Sun, F. Chen, K. Chen, Z. Hu, and Y. Cao, "Integrated Optical Electric Field Sensor From 10 kHz to 18 GHz," *IEEE Photonics Technology Letters,* vol. 24, no. 13, pp. 1106-1108, 2012.

[21] Y. N. Wijayanto, H. Murata, and Y. Okamura, "Electro-optic microwave-lightwave converters utilising quasi-phase-matching array of patch antennas with gap," *Electronics Letters,* vol. 48, no. 1, pp. 36-38, 2012.

[22] R. B. Waterhouse and D. Novak, "Integrated antenna/electro-optic modulator for RF photonic front-ends," in *2011 IEEE MTT-S International Microwave Symposium*, 2011, pp. 1-4.

[23] R. Himmelhuber *et al.*, "A Silicon-Polymer Hybrid Modulator—Design, Simulation and Proof of Principle," *Journal of Lightwave Technology,* vol. 31, no. 24, pp. 4067-4072, 2013.

[24] A. Hosseinzadeh, "Linear Ring Resonator Modulator for Microwave Photonic Links," PhD, Michigan Technological University, Ann Arbor, 10929521, 2018.

[25] H. Nishihara, M. Haruna, and T. Suhara, *Optical Integrated Circuits*. McGraw-Hill, 1989, p. 14.

[26] B. Ahcene and N. Merabtine, *Analysis of radiation patterns of rectangular microstrip antennas with uniform substrate*. 2005.

[27] Y. Enami, A. Seki, S. Masuda, T. Joichi, J. Luo, and A. K. Y. Jen, "Bandwidth Optimization for Mach–Zehnder Polymer/Sol–Gel Modulators," *Journal of Lightwave Technology,* vol. 36, no. 18, pp. 4181-4189, 2018.

[28] C. A. Balanis, *Antenna Engineering Analysis and Design*, Second ed. John Wiley and Sons, 1997, pp. 250-251.

[29] S. Wi, Y. Lee, and J. Yook, "Wideband Microstrip Patch Antenna With U-Shaped Parasitic Elements," *IEEE Transactions on Antennas and Propagation,* vol. 55, no. 4, pp. 1196-1199, 2007.

[30] F. Hu, J. Song, and T. Kamgaing, "Modeling of multilayered media using effective medium theory," in *19th Topical Meeting on Electrical Performance of Electronic Packaging and Systems*, 2010, pp. 225-228.

[31] B. Saleh and M. Teich, *Fundamentals of Photonics*, 1 ed. John Wiley and Sons, 1991, pp. 697-700.

[32] J.-M. Liu, *Photonic Devices*. Cambridge University Press, 2005.

[33] E. L. Wooten *et al.*, "A review of lithium niobate modulators for fiber-optic communications systems," *IEEE Journal of Selected Topics in Quantum Electronics,* vol. 6, no. 1, pp. 69-82, 2000.

[34] Lumera Corporation, "Applications of Electro-optic Polymers and Devices: Breaking the High Frequency, Broad Bandwidth Barrier," February 2008, Available: https://pdfs.semanticscholar.org/caae/76e8a76202f7b56786eb0b75b8336562d0fb.pdf.

[35] Soluxra LLC, "Processing Description of SEO100C," datasheet, June 2015, unpublished.

[36] M. Lee, O. Mitrofanov, H. E. Katz, and C. Erben, "Millimeter-wave dielectric properties of electro-optic polymer materials," *Applied Physics Letters,* vol. 81, no. 8, pp. 1474-1476, 2002.

[37] L. R. Dalton *et al.*, "From molecules to opto-chips: organic electro-optic materials," *Journal of Materials Chemistry,* 10.1039/A902659B vol. 9, no. 9, pp. 1905-1920, 1999.

[38] M. D. Watson, "Electrical Transfer Function and Poling Mechanisms for Nonlinear Optical Polymer Modulators," PhD, Electrical and Computer Engineering, University of Alabama in Huntsville, Huntsville, Alabama, 2005.

[39] R. A. Soref, J. Schmidtchen, and K. Petermann, "Large single-mode rib waveguides in GeSi-Si and Si-on-SiO/sub 2," *IEEE Journal of Quantum Electronics,* vol. 27, no. 8, pp. 1971-1974, 1991.

[40] S. P. Pogossian, L. Vescan, and A. Vonsovici, "The single-mode condition for semiconductor rib waveguides with large cross section," *Journal of Lightwave Technology,* vol. 16, no. 10, pp. 1851-1853, 1998.

[41] A. Melloni, R. Costa, G. Cusmai, and F. Morichetti, *The role of index contrast in dielectric optical waveguides*. 2009.

[42] X.-L. Zhao *et al.*, "Optimized design and fabrication of nanosecond response electro–optic switch based on ultraviolet-curable polymers," *Chinese Physics B,* vol. 24, no. 4, 2015.

[43] J. A. Woolam Co., *Guide to Using WVASE32 Spectroscopic Ellipsometry Data Acquisition and Analysis Software*. Lincoln, NE: J. A. Woolam Co., Inc., 2008, p. 8.

[44] B. Pen-Cheng Tsou, "Electrooptic Mach-Zehnder Modulators in Galliam Arsenide," Master's of Science, Electtcial Engineering, University of British Columbia, 1993.

[45] S. M. Lindecrantz and O. G. Hellesø, "Estimation of Propagation Losses for Narrow Strip and Rib Waveguides," *IEEE Photonics Technology Letters,* vol. 26, no. 18, pp. 1836-1839, 2014.

[46] A. R. Tynes, A. D. Pearson, and D. L. Bisbee, "Loss Mechanisms and Measurements in Clad Glass Fibers and Bulk Glass," *Journal of the Optical Society of America,* vol. 61, no. 2, pp. 143-153, 1971/02/01 1971.

[47] O. Min-Cheol *et al.*, "Recent advances in electrooptic polymer modulators incorporating highly nonlinear chromophore," *IEEE Journal of Selected Topics in Quantum Electronics,* vol. 7, no. 5, pp. 826-835, 2001.

[48] D. Guerin, S. Jackson, and J. Kelly, "Passive Direction Finding A Phase Interferometry Direction Finding System for an Airborne Platform," Worchester Polytechnic Institute 2012.

[49] A. R. Webster, J. Jones, and K. J. Ellis, "Direction finding using a linear three-element interferometer approach," *Radio Science,* vol. 37, no. 6, pp. 7-1-7-6, 2002.

[50] R. M. O'Donnel, "Radar Transmitter/Receiver," in *Introduction to Radar Systems,* Lincoln Laboratory MIT, 2018, http://www.ll.mit.edu/outreach/introduction-radar-systems.

[51] A. Hosseinzadeh and C. T. Middlebrook, "Analog Signal Modulation Using an All-Polymer Ring Resonator Modulator," *Journal of Lightwave Technology,* vol. 37, no. 3, pp. 755-760, 2019/02/01 2019.

[52] S. Michel, J. Zyss, I. Ledoux-Rak, and C. T. Nguyen, *High-performance electro-optic modulators realized with a commercial side-chain DR1-PMMA electro-optic copolymer* (SPIE OPTO). SPIE, 2010.

[53] T. Kawanishi, "Parallel Mach-Zehnder modulators for quadrature amplitude modulation," *IEICE Electronics Express,* vol. 8, no. 20, pp. 1678-1688, 2011.

[54] T. Sakamoto, A. Chiba, and T. Kawanishi, "50-Gb/s 16 QAM by a quad-parallel Mach-Zehnder modulator," in *33rd European Conference and Exhibition of Optical Communication - Post-Deadline Papers (published 2008)*, 2007, pp. 1-2.

[55] T. A. Milligan, *Modern Antenna Design*, 2nd ed. John Wiley and Sons, 2005.

[56] COMSOL, "Wave Optics Module User's Guide," 2013.

[57] Y. Enami, G. Meredith, N. Peyghambarian, and A. K. Y. Jen, "Hybrid electro-optic polymer/sol–gel waveguide modulator fabricated by all-wet etching process," *Applied Physics Letters,* vol. 83, no. 23, pp. 4692-4694, 2003.

[58] X. Zhang *et al.*, "Integrated Photonic Electromagnetic Field Sensor Based on Broadband Bowtie Antenna Coupled Silicon Organic Hybrid Modulator," *Journal of Lightwave Technology,* vol. 32, pp. 3774-3784, 2014.